Ultra-fast laser ablation dynamics using beam shaping

Dashdeleg Baasanjav

Cover
Cover photo/illustration with an explanation

Baasanjav, Dashdeleg

Ultra-fast ablation dynamics using beam shaping
D. Baasanjav - Utrecht
Universiteit Utrecht
Faculteit Bètawetenschappen
Departement Natuur- en Sterrenkunde
Thesis Universiteit Utrecht - With a summary in Dutch

Ultra-fast laser ablation dynamics using beam shaping

De dynamica van ultrasnelle laser ablatie met gevormde bundels

(met een samenvatting in het Nederlands)

Proefschrift

ter verkrijging van de graad van doctor aan de
Universiteit Utrecht
op gezag van de
rector magnificus, prof. dr. H.R.B.M. Kummeling,
ingevolge het besluit van het college voor promoties
in het openbaar te verdedigen op
donderdag 4 juni 2020 des middags te 12.45 uur

door

Dashdeleg Baasanjav

geboren op 19 augustus 1987
te Ulaanbaatar, Mongolië

Promotor:	Prof. dr. A. P. Mosk
Copromotor:	Dr. D. van Oosten

To the people who supported and believed in me
during this amazing journey of ultrafast PhD

Contents

1 Introduction

Abstract. The invention of high power lasers with extremely short pulses ranging from femto to nanosecond duration opened a plethora of new studies and industrial applications ranging from laser based surgery, laser processing of materials in the semiconductor industry and photonics and even to defense applications. However, the spatial distribution of the laser light field is mostly limited to Gaussian shapes, which can prove restrictive for many applications. In this thesis, we study a combined approach of ultrafast laser ablation with spatial beam shaping, which not only is interesting in terms of applications, but also opens up new roads to understand the fundamental physical process of highly non-linear interaction of light and matter. To prelude, we provide an overview of the field and the theoretical and experimental background necessary for the main part of the thesis.

1.1 Surface ablation

The laser is one of the hallmark inventions based on quantum physics. Lasers are getting used more and more in every aspect of life, ranging from simple applications such as barcode reading, laser printing and laser projection to industrial as well as defense applications. Fiber-optics communication technology enables world-wide information sharing with high speed. Satellite based internet technology is being developed currently, which is possible through use of lasers. High power lasers are starting to get used for defense applications such as directed-energy weapons. In semiconductor lithography, extreme ultraviolet (EUV) light, where EUV plasma source is pumped by high power pulsed lasers, drives Moore's law into the next decades.

The invention of chirped pulse amplification in 1980s for which the 2018 Nobel Prize in Physics was awarded to Gérard Mourou and Donna Strickland, opened up whole new possibilities to generate ultrashort laser pulses with powers up to the petawatt level without damaging the gain medium, making it possible to study fundamental light-matter interactions with extreme spatial

and temporal resolutions [1]. This has led to fascinating studies in attosecond science [2]. High-order harmonic generation in gas medium, pumped by the intense and femtosecond laser pulses, made it possible to produce coherent extreme ultraviolet pulses with attosecond pulse duration [3]. The attosecond pulses are used to investigate ultrafast electron dynamics in various types of materials and molecules [2] such as the measurement of the delay in photoemission [4, 5], the observation of electon tunneling ionization [6] and the measurement of the electron localization process in H_2 and D_2 molecules after being excited by the attosecond pulses [7], to name a few. Due to the extreme focused intensity $> 10^{18}$ W/cm^2, generated by the ultrafast lasers, studies in relativistic optics and even ultra-relativistic optics are now also possible as the enormous amount of energy that is deposited into the electrons and protons in a material by the laser pulse can accelerate them up to relativistic speeds [1]. On the other hand, as ultrashort pulsed lasers are now available as robust and turn-key system, they are also an excellent technology for the ablation of metals [8, 9], semiconductors [10, 11], dielectrics [12] and even biological materials [13]. Femtosecond laser ablation of material surfaces has gathered particular interest from the scientific community as well as industry, especially the semiconductor and the medical industry, due to its ability to remove material with extreme precision and low collateral damage. Therefore, it is important to understand the physical phenomena behind femtosecond laser ablation of silicon and aqueous materials.

The underlying physical processes behind femtosecond laser ablation are, in contrast to the case of ns and μs pulse ablation, well separated over different time scales [13–15], due to the ultrafast energy deposition and the non-linearity of the processes. Although water, which is the main component in aqueous materials, is an insulator and silicon is a semiconductor, we can in both cases categorize the fundamental processes during femtosecond laser ablation into four regimes based on the time scale of each process: (1) generation/heating of free carriers (100's fs), (2) heating of ions/molecules (1 - 10 ps), (3) expansion of vapor (ablation plume) (ps - ns), and (4) motion of liquid material (μs - ms). In the first few hundred fs, the laser pulse couples to the material through multi-photon absorption and impact ionization, which starts to generate a free carrier plasma [16]. Unlike ns and μs pulses, the optical properties of the material change profoundly during the pulse propagation, mainly due to the presence of dense electron plasma, which in turn influences the pulse propagation. Even though the time scale of the pulse is short, the carrier-carrier

collision time is even shorter [17], so we can assume that the free carriers inside the plasma remain in thermal equilibrium with each other. On the ps time scale, the electron plasma starts to couple to the lattice or the motion of the atoms/molecules and heat diffusion takes place. The resulting super heated material will expand, creating an ablation plume, containing electron plasma, ions and neutral atoms. In the case of semiconductors, a thin layer of material underneath the plume will be in the liquid state. From ps to ns, the ablation plume expands supersonically in the normal direction [18]. The recoil pressure will cause the liquid material to move on a μs to ms time scale. The motion of the liquid can be particularly violent, leading to crowning and splashing, as evidenced by the ablation aftermath [19]. Understanding the physical mechanism behind material removal, or in other words what exactly drives the liquid motion during ablation, is an extremely important and challenging problem. There are two processes that can lead to liquid motion in this case: the aforementioned strong recoil pressure from the expanding ablation plume and the ejection of liquefied material due to a gradient of the surface tension, the so-called Marangoni effect [20]. Studying expansion dynamics of the ablation plume is essential in figuring out which process is dominant during material removal. However, so far most studies of on the ablation plume dynamics have been done under weak focusing condition [18, 21–23], which is fundamentally different from strong focusing condition, as we will argue this in next sections. Moreover, the understanding of femtosecond ablation under strong focusing condition is vital due to its high spatial resolution and low collateral damage, which is indispensable for applications that require ultra precision and material removal efficiency such as cell surgery [24] and silicon wafer ablation [25].

1.2 Ultrafast time-resolved imaging: pump and probe microscopy

The most powerful tools to study femtosecond ablation dynamics are so-called time-resolved pump-probe schemes [18, 24, 26–30]. Material is excited by an energetic pump pulse, from an amplified laser source. A part of the pulse is delayed and used to image the material either in reflection, transmission or scattering mode. This probe pulse is often generated by frequency doubling a part of the laser pulse. The time delay is controlled by an optical delay

line for short time delays, typically less than 100 ns. For longer delays, the probe pulse can also be derived from a second laser, in which case the delay is generated by an electronic circuit.

These techniques can be further categorized into two groups based on imaging method. One is time-resolved side-imaging including absorption imaging (also called shadowgraphy) [18,24,26], although one could also use phase contrast imaging (using for instance the Schlieren or Zernike methods). Many studies of femtosecond ablation involving weak focusing are done by time-resolved shadowgraphy [18,24], where a pump pulse is focused onto the sample in one direction, while a probe pulse is impinged on the sample from a direction perpendicular to the pump and the transmitted probe light is captured by a camera. However, shadowgraphy is not suitable for ablation studies with a strong focusing, as the small lateral size of the plume does not have enough optical thickness to give sufficient optical contrast. For example, in the case of strong focusing, the diameter of the shockwave during the first few ns is around 30 μm [26, 30] while it is around 2 mm in the case of the weak focusing [18]. Seminal work shown in Ref. [26] shows the ablation dynamics with strong focusing inside bulk water using shadowgraphy. To get sufficient signal, the authors implemented an averaging method where every image is actually an average of 100 images, and even then, the signal to noise ratio is rather poor. Another method is time-resolved reflectivity imaging [27–30], where both pump and probe pulse are sent through same focusing element. The reflected probe light is sent back to the element and recorded by a camera. This has several advantages over the side-imaging method. Due to comparatively large change in reflectivity coming from ablation features [30], it is possible to perform single-shot ablation studies with high spatial resolution. It is also much easier to implement experimentally and compatible with high numerical aperture (NA) microscopy, yielding a high spatial resolution.

Here, we describe the experimental setup used in this thesis and provide a general description about its main aspects. Our setup is based on Ref. [30] with additions that are discussed in Chapters 2 and 4. We use the above mentioned time-resolved reflectivity imaging, also called transient reflectivity microscopy, with a high NA objective[1] to study dynamics of ultrafast laser ablation at a water/air interface. Fig. 1.1 shows the schematics of the setup. A femtosecond pulse with a pulse duration of 150 fs and a wavelength of 800

[1] Nikon CFI60, 100x, NA=0.8

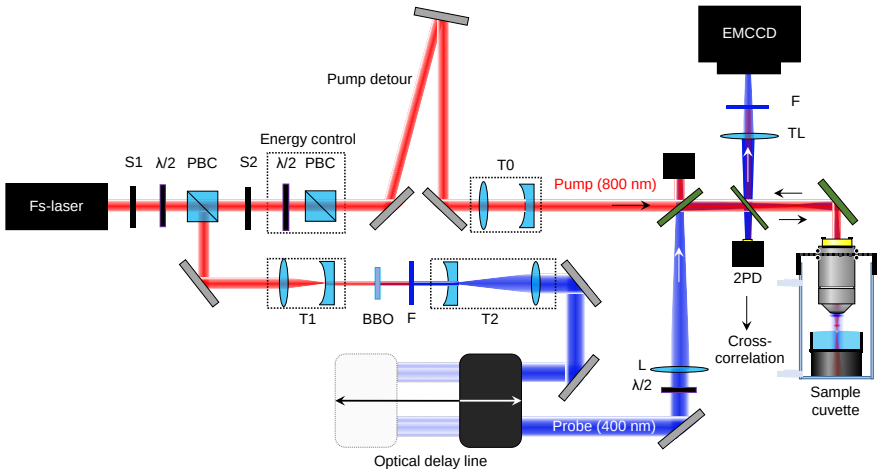

Figure 1.1: Transient reflectivity microscopy setup. Adapted with permission from Ref. [30].

nm, depicted in red, is generated by a femtosecond regenerative amplifier[2]. This pulse is split into two pulses, one is the pump pulse used to excite the water surface and the other one is a probe pulse used to image the surface after the excitation. The probe pulse with a wavelength of 400 nm, depicted in blue, is generated by frequency doubling one of the split pulses with a BBO (beta barium borate) crystal. A $\lambda/2$ waveplate and a polarizing beam splitter are used to control pump pulse energy. During actual experiments, neutral density filters, not depicted in the figure, are used to modify the pulse energy in calibrated steps. An optical delay line is used to precisely control the delay time between the pump and probe pulse. The delay time can range from 10 fs to 100 ns. In this thesis, we mostly use a fixed delay of 10 ns to study the gas expansion regime. The pump beam is then strongly focused by the objective onto the sample, resulting in a beam waist of 3.1 μm [30]. The probe beam is focused onto the back focal plane of the objective thus providing wide field illumination of the sample. The reflected probe light is then imaged on an electron multiplying CCD camera[3] using a f=300 mm tube lens (TL). Filters (F)[4] are placed inside the setup (inside the probe path and in front of the camera) so that there is no light with a wavelength of 800 nm

[2]Hurricane, Spectra-Physics
[3]Andor, Ixon 885
[4]$\lambda_0 = 400$ nm, $\Delta\lambda_{\mathrm{FWHM}} = 10$ nm

in the probe path and only reflected probe light is collected by the camera. Fig. 1.2(b) shows a cuvette in which the objective and the sample are mounted. The gaseous atmosphere inside the cuvette can be changed with a circulating system with a supply and an exhaust.

Now we discuss some previous results obtained with this setup that preceded this thesis [30]. Fig. 1.2(c) shows typical transient reflectivity images measured in an air atmosphere with time delays from 0.2 ps to 100 ns, showing the underlying dynamics of the ablation process. As illustrated in Fig. 1.2(a), the processes involved in fs laser ablation at a water/air interface are well separated in time. During first few hundred fs to a ps, the laser pulse excites water molecules and ionizes them, producing a dense electron plasma, which result in bright spots at the center of images (images c1-c3). Then the electron plasma starts to thermalize with the atomic nuclei and thermal energy of the plasma dissipates into the surrounding water medium (images c4-c6). This energy redistribution leads to heating of the water and thus to evaporation, which produces rapidly expanding vapor that show up as black disks at the center of images. This happens rapidly during 20 ps to 100 ns (images c7-c18).

Fig. 1.3(a)-(e) show representative images from different time scale regimes. Corresponding azimuthal averages (f)-(j) and illustrations of the physical processes involved (k)-(o) are also shown. Fig. 1.3(a), (b) and (e) are particularly interesting. The strong increase in relative reflectivity in Fig. 1.3(a) and (b) is due to the dense electron plasma [30, 31]. However, there is a reflectivity dip in the center of Fig. 1.3(b), which is attributed to the start of the evaporation [30, 31] already at 2 ps. From Fig. 1.3(e) and (j), one can see there is a sharp edge surrounding the ablation plume and shockwave-like feature. This feature resembles a surface ripple in a normal-incidence imaging method. However, this is not a surface ripple because the surface ripples would not depend on the surrounding gas atmosphere whereas the shockwave-like feature we observe does depend on the surrounding gas atmosphere, as shown in Fig. 1.4. The expansion of the plume is expected to be highly elongated in a vertical direction [30], shown in Fig. 1.3(o), which will be further discussed in next section.

As shown in Fig. 1.4, the authors of Ref. [30] recorded transient reflectivity images in the presence of different gas atmospheres. The authors use 1,1,1,2 tetrafluoroethane (TFE), air, and Helium with densities 4.25 mg/cm^3, 1.20 mg/cm^3, and 0.18 mg/cm^3 respectively. From the figure, one can see that the shockwave-like feature is more visible for denser gas atmosphere. This can

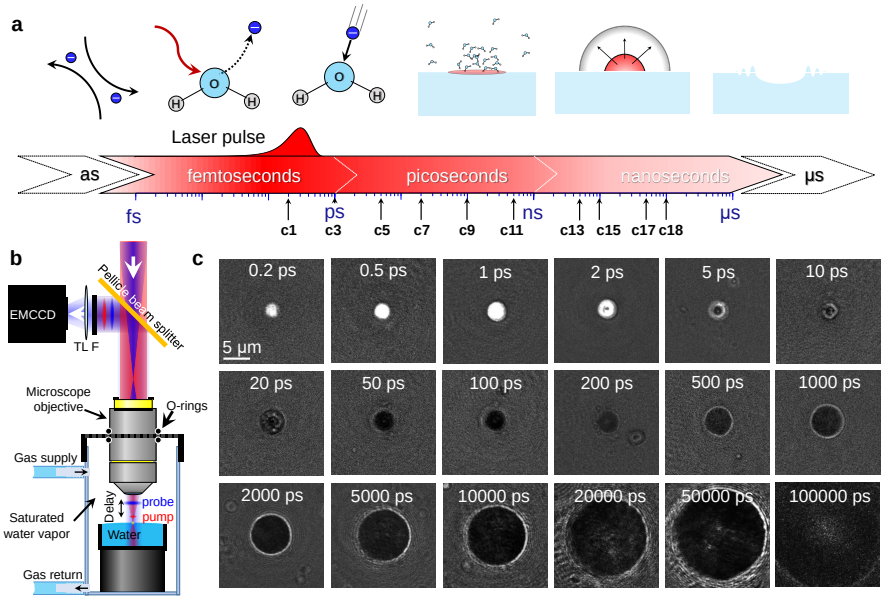

Figure 1.2: (a) Time-line of ultrafast ablation of water and illustration of involved processes. Representative images from (c) are indicated with arrows labelled c1 to c18 at corresponding time-line positions. (b) Detailed schematics of the sample cuvette. (c) Typical transient reflectivity images recorded at pump-probe delays from 0.2 ps to 100 ns. Pump pulse fluence is 25 J/cm^2. Reproduced with permission from Ref. [30].

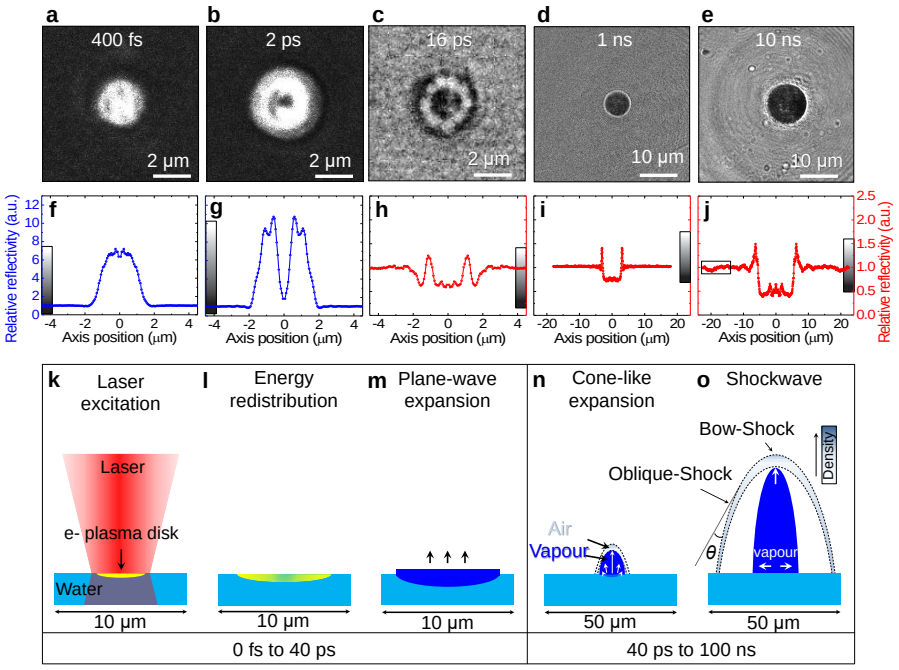

Figure 1.3: (a)-(e) Transient reflectivity images from different time scale regimes. Corresponding radial averages (f)-(j) and physical processes (k)-(o) are shown. Reproduced with permission from Ref. [30].

be understood as the heavier gases have a lower sound velocity, so the mach number of initial plume expansion is higher, leading to a sharper discontinuity between the expanding plume with supersonic (in air) or hypersonic speed (in TFE) and the surrounding atmosphere, creating much more optical contrast. The associated shockwave will obviously also be stronger. Another important thing to note is that the size of the ablation plume stays roughly the same for all the gas atmosphere at each time delay, from 500 ps to 10 ns. This suggests that the dynamics of the lateral expansion of the ablation plume is only weakly dependent on the atmosphere. However, the dynamics of the vertical expansion should obviously be different as the expansion slows down more quickly for heavier gases due to the fact that the expanding plume gathers up mass faster. This will be discussed further in Section 1.6. A study on the vertical expansion requires the side-imaging methods which, as discussed before, are unpractical under strong focusing conditions. An approach using a strongly elongated pump pulse will be discussed as an outlook of the thesis.

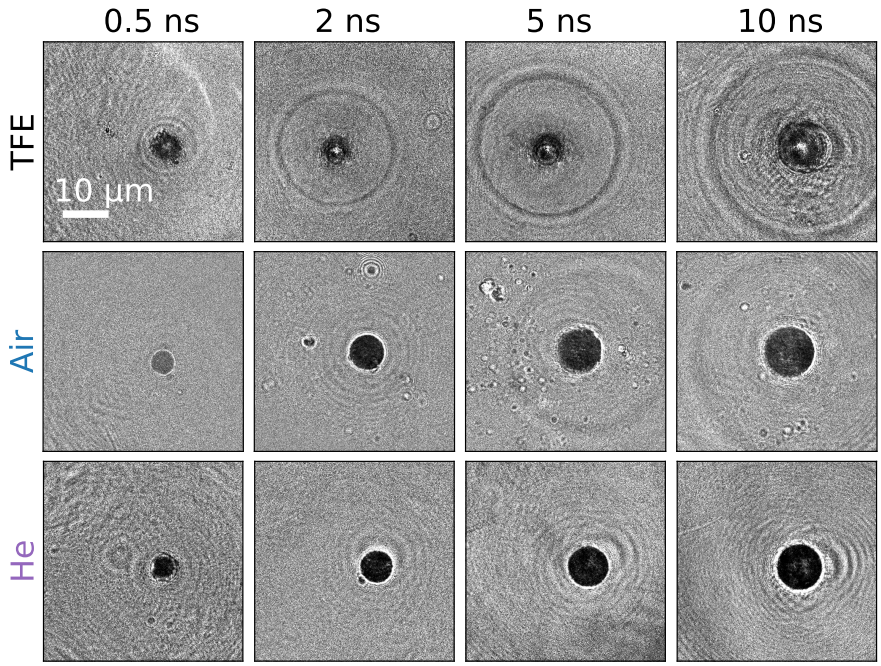

Figure 1.4: Atmosphere influence on ablation dynamics. Transient reflectivity images of expanding vapor in the presence of tetrafluoroethane (TFE), Air and Helium. Adapted with permission from Ref. [30].

1.3 FDTD simulation of electron dynamics during the excitation

As previously discussed in Sections 1.1 and 1.2, ablation of liquids and semiconductors are a combination of different processes that are well separated in time. In this section, we provide a general description of a numerical model simulating the electron plasma dynamics and initial energy deposition process during the first ps of water ablation, which is a crucial first step to understand the eventual ablation plume expansion. The model was developed by our group and a full description of it can be found in Refs. [31–33]. In this thesis, we use the model to calculate the heat deposited into the material by the excitation pulse. Here we discuss the relevant aspects of the model.

As a fs laser pulse propagates through the material, it changes the material properties by creating a dense electron plasma in the impact region. The plasma in turn affects the optical properties of the material, thereby altering the pulse propagation. This problem can be described by a coupled set of equations, specifically the Maxwell equations and material equations. The Maxwell equations are used to calculate the optical propagation of the pulse through the material. The result of this calculation is used as input for the material equations, from which the optical properties such as susceptibility and electric conductance of the material are extracted. The extracted optical properties are then inserted back into the Maxwell equations.

The Maxwell equations in a material are

$$\begin{aligned} \nabla \times \mathbf{E} &= -\frac{\partial \mathbf{B}}{\partial t}, \quad \nabla \cdot \mathbf{D} = \rho_{\mathrm{f}}, \\ \nabla \times \mathbf{H} &= \frac{\partial \mathbf{D}}{\partial t} + \mathbf{j}_{\mathrm{f}}, \nabla \cdot \mathbf{B} = 0, \end{aligned} \tag{1.1}$$

where $\mathbf{j}_{\mathrm{f}}$ is the free current density and ρ_{f} is the free charge density. The auxiliary fields are given as

$$\mathbf{D} = \epsilon_0 \mathbf{E} + \mathbf{P}, \mathbf{H} = \frac{1}{\mu_0}\mathbf{B} - \mathbf{M}. \tag{1.2}$$

For optical frequencies, we can neglect the magnetic permeability of the material and consider only the electric susceptibility, which is in general a function of both a position and time. The effects of free currents and charges can be taken into account implicitly in the electric susceptibility [33]. In that case, to avoid double counting, the free currents and charges are removed from the

Maxwell's equations, which yields

$$\frac{\partial \mathbf{H}(\mathbf{r},t)}{\partial t} = -\frac{1}{\mu_0}\nabla \times \mathbf{E}(\mathbf{r},t), \tag{1.3}$$

$$\frac{\partial \mathbf{E}(\mathbf{r},t)}{\partial t} = \frac{1}{\epsilon_0 \epsilon(\mathbf{r},t)}\nabla \times \mathbf{H}(\mathbf{r},t), \tag{1.4}$$

from which the electric and magnetic field in the material are solved using a two-dimensional finite-difference time-domain (2D FDTD) routine [32, 33].

When the pulse interacts with an unperturbed material surface, it excites electrons from the valence to the conduction band through strong field (multi-photon) absorption, as there are no free electrons present in the conduction band for insulators and single-photon absorption is impossible as the photon energy is too low. On top of that, free-carrier absorption (inverse bremsstrahlung) creates additional electronic excitations in the conduction band. Once the electrons in the conduction band have sufficient thermal energy, they can produce more free electrons by collisional excitation, a process known as the avalanche ionization. All these processes can be captured by the multiple rate equation (MRE) method [12, 16, 34], in which we discretize the conduction band into effective energy levels spaced by the photon energy. The method is summarized in the equations

$$\begin{aligned}
\dot{\rho}_0 &= -W_{1\mathrm{pt}}\rho_0 + W_{\mathrm{SFI}} + 2\alpha\rho_k, \\
\dot{\rho}_1 &= -W_{1\mathrm{pt}}\rho_1 + W_{1\mathrm{pt}}\rho_0, \\
&\vdots \\
\dot{\rho}_{k-1} &= -W_{1\mathrm{pt}}\rho_{k-1} + W_{1\mathrm{pt}}\rho_{k-2}, \\
\dot{\rho}_k &= -\alpha\rho_k + W_{1\mathrm{pt}}\rho_{k-1},
\end{aligned} \tag{1.5}$$

where ρ_i is the electron number density at ith energy level and α (1 fs^{-1}) is the avalanche ionization coefficient [31]. The total number of energy levels is $k = U_{\mathrm{eff}}/\hbar\omega$, where U_{eff} is the ionization potential of the material and $\hbar\omega$ is the photon energy. $W_{1\mathrm{pt}}$ is the one-photon absorption coefficient and W_{SFI} is the strong-field ionization rate, which is computed as a function of the electric field strength at the pulse wavelength [31]. The electron plasma temperature and number density can be computed using

$$k_B T = \frac{2}{3}\frac{\sum_{j=0}^{k} j\hbar\omega\rho_j}{\sum_{j=0}^{k}\rho_j} \quad \text{and} \quad \rho(\mathbf{r},t) = \sum_{j=0}^{k}\rho_j(\mathbf{r},t), \tag{1.6}$$

where k_B is the Boltzmann constant. Typically one finds that there are 0.1 - 1 excited electron per atom/molecule at a temperature of several 10000 Kelvin, for typical ablation conditions [35]. Therefore, it is justified to use a Boltzmann distribution to describe the electron plasma [35]. The scattering rate of the electron plasma is a sum of an electron-electron Γ_{e-e} and an electron-phonon Γ_{e-p} scattering rate as

$$\Gamma(\mathbf{r},t) = \Gamma_{e-p}(\mathbf{r},t) + \Gamma_{e-e}(\mathbf{r},t). \tag{1.7}$$

The Γ_{e-p} is 1 fs^{-1} [31], while the Γ_{e-e} is given as [34]

$$\Gamma_{e-e}(\mathbf{r},t) = \frac{4\pi\epsilon_0}{e^2}\sqrt{\frac{6}{m_e}}(k_B T)^{3/2}. \tag{1.8}$$

Here e and m_e are the electron charge and mass respectively. Following Refs. [31–33], the dielectric function can be computed using

$$\epsilon(\mathbf{r},t) = \epsilon_{\text{mat}} - \frac{\omega_p^2(\mathbf{r},t)}{\omega^2 + i\omega\Gamma(\mathbf{r},t)} + \frac{3}{4}\chi_3|E(\mathbf{r},t)|^2, \tag{1.9}$$

where ϵ_{mat} is the dielectric constant of unexcited material at the pulse wavelength, χ_3 is the third-order nonlinear susceptibility and $\omega_p^2(\mathbf{r},t) = e^2\rho(\mathbf{r},t)/m_e\epsilon_0$ is the plasma frequency.

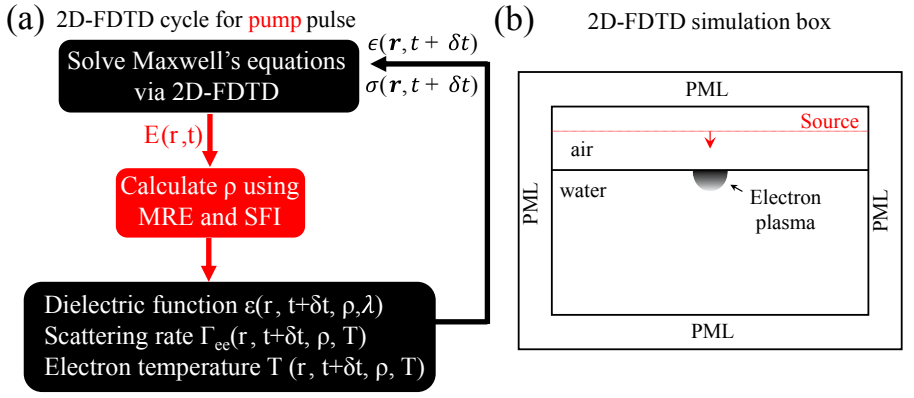

Figure 1.5: (a) Schematics of a calculation routine with an excitation pulse. (b) Simulation box. PML denotes the perfectly matched layer that minimizes the reflection. Adapted with permission from Ref. [31].

Fig 1.5(a) shows a schematic of one cycle of the 2D FDTD routine. At every half optical cycle δt, the electric field distribution is calculated. Then

the model updates the MRE and the electron plasma density is obtained. Using those values, we calculate the dielectric function and plasma conductivity based on Eq. 1.9. These values are used for the next cycle [32, 33]. In Fig 1.5(b), the 2D simulation box (z-x) we used is shown. The air/material interface is located at z=0. Perfectly matched layers (PML) are used to minimize the reflected fields coming from the edges of the box.

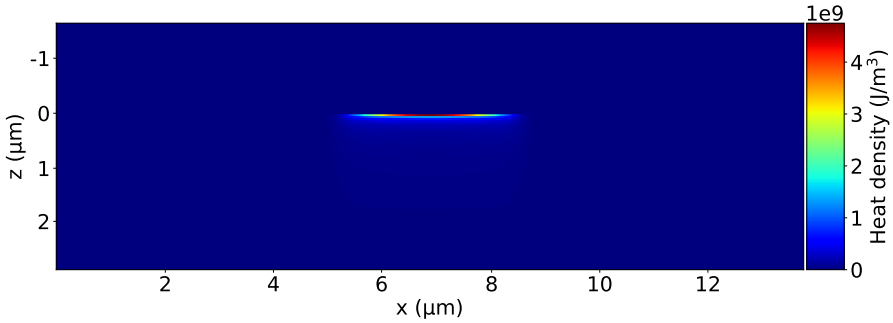

Figure 1.6: Heat distribution inside water at 700 fs after the pump pulse peak intensity. The pump pulse fluence is 21 J/cm^2.

In Fig. 1.6, we show a calculation result of a heat distribution inside water as the material, relevant to Chapter 2. We compute the heat distribution at 700 fs after the pump pulse peak intensity whose fluence is 21 J/cm^2. Based on Eq. 1.6, the heat distribution inside the material is taken as $3/2k_BT\rho$, which is the kinetic energy of the electron plasma. The FDTD calculations are done in two dimensional Cartesian coordinate system. However, when we calculate the absorbed energy we assume the material has a 3D cylindrical symmetry [32, 33]. Thus, we do 3D cylindrical integration of the total heat distribution to compute the absorbed energy. We assume that the thermal energy of the plasma has not dissipated into surrounding bulk water as the evaporation of the water molecules happens in ps time scale, shown in Fig. 1.2. The energy of the electron plasma is what drives the eventual plume expansion during the first 10 ns because the recombination of the electrons and the ions does not happen significantly even within 30 ns [36]. Although water does not have an electronic band structure strictly, the model describes well the water ablation. It is originally developed for a fused silica [32, 33], which is also an amorphous material.

1.4 Beam shaping

Beam shaping, changing the structure of a coherent light beam in space and time into desired patterns utilizing non-trivial optics, has become a powerful tool to investigate light-matter interaction [37, 38]. There are different ways to shape laser beams [37,38]. At the source, intra-cavity mode control is used to create ultra-pure modes for high-intensity laser beams [37]. Outside the source, various static optical elements such as diffractive and refractive optical elements are used to shape the light field [38]. With recent developments of liquid crystal spatial light modulators, adaptive optics has emerged as a powerful way to control the light field dynamically due to its high versatility and ease of implementation compared to its static counterparts [39]. Control of each aspect of light such as temporal, spatial distribution and polarization brings benefits. For example, temporal pulse shaping is used to compensate dispersion due to pulse propagation over long distance [37]. Radially and azimuthally polarized beams are used to create tight foci with smaller beam waists compared to a Gaussian beam [37]. Spatial beam shaping is used to create custom intensity light fields at a desired plane [37]. In this thesis, we focus on spatial beam shaping.

Spatial beam shaping has been utilized in various fields in the form of holographic beam shaping after the development of liquid crystal spatial light modulators. For example, in atomic physics it is used for creating holographic atomic traps [40–42]. In biophysics, it is used for creating optical tweezers [43, 44], producing integrated microfluidic systems based on two-photon polymerization [45] and inducing a temperature gradient on gold nanoparticles, *i.e.* thermoplasmonics [46]. In optics, it is used for imaging through multiple scattering materials [47]. In ablation, it is mainly used for laser processing of materials with spatially shaped laser pulses [48], for instance to generate multiple excitation spots to reduce processing time [49, 50] and to produce foci with extended depth of field to create nano-scale holes [48] and material removal with spatially shaped foci such as a donut and TopHat [35, 51, 52]. We use spatial beam shaping in Chapters 2 and 4 of this thesis.

1.5 Outline of this thesis

In this thesis, we present experimental and numerical studies on applications of the spatial beam shaping in ultrafast laser ablation of different types of

material surfaces. This thesis is organized as follows:

In the previous **Sections**, we have discussed relevant recent work done by our group and the others.

In **Section 1.6**, related to the plume expansion dynamics, we present a derivation and numerical study of two point blast models [53, 54], originally developed for three dimensional expansions, in two and one dimensional expansion. Based on the results, we clarify the difference between the strong and the weak focusing regimes in ablation.

In **Chapter 2**, we simultaneously induce the double excitations at a water/air interface with a SLM. By dynamically changing the distance between the excitations, we map out the velocity field of the gas front at two different pulse energies. Our FDTD calculation of absorbed energies suggests that the plume expansion dynamics deviates from the standard point blast model [53] often used to describe the expansion.

In **Chapter 3**, we experimentally study the ablation of gel and water as both have similar optical and material properties. Also the gel provides an aftermath, which would not be possible in the ablation of water as the surface recovers after every pulse excitation. During the first 10 ns, we find the similar expansion dynamics in both water and gel over a large range of pulse energies. We measure the volume of the gel craters produced during ablation with an optical profilometer and provides an estimate on the removed mass. To get more insight, we calculate the absorbed energies corresponding to the pulse energies. We find a surprisingly similar trend in the removed gel volumes and the absorbed energies.

In **Chapter 4**, we present a beam shaping method for the ablation of silicon wafers. We numerically study an algorithm [55] used to create high-fidelity TopHat beam shapes. We experimentally create the beam shapes at the intermediate image plane of our setup, and study its light efficiency and root mean squared errors. We then demonstrate the TopHat patterns through a high NA objective.

Finally, in **Chapter 5**, we summarize the results of the thesis and provide an outlook on future studies.

1.6 Point blast models

As discussed in the previous sections, transient reflectivity microscopy allows us to image the ablation plume and the shockwave-like features surrounding

it. To interpret such images, it would be helpful to have a model to describe the expansion of the plume. In this section, we discuss two models that could describe the expansion physics and present new calculations for 2D and 1D expansion. We then comment on how we define the strong and weak focusing in ablation.

A model often used in the ablation is the Sedov-Taylor (ST) model, first derived assuming a spherical blast geometry [53]. However, as described in Section 1.2, the plume expansion during ablation at the water/air interface has highly elongated, non-spherical geometry. So it would be interesting to derive the ST model for a 1D expansion. For completeness, we will also derive the 2D case. We will do so with a highly simplified model which, unlike the full derivation by ST, does not compute the radial dependence of the pressure, temperature and density, but rather only determines the scaling as a function of time. This approach is commonly used in literature on supernova remnant (SNR) physics [54]. Drawing inspiration from SNR physics, we also discuss the free expansion model that is used to describe the initial expansion phase of the supernova explosion [54]. We numerically integrate our models in three, two, and one dimensions for the time scales relevant to the plume expansion and discuss the transition between these models.

1.6.1 Sedov-Taylor model in non-spherical geometries

The standard ST model describes the spherically symmetric expansion of a point-like blast. Here we derive scaling results in 2D and 1D. To the best our knowledge, these derivations have not been published before.

Sedov-Taylor model in 2D expansion

If E is the initial energy released by a point blast explosion and we assume that all energy is converted into kinetic energy, we can write it as

$$E = \frac{1}{2}mv^2. \tag{1.10}$$

The moving mass m is assumed to be the mass of the surrounding medium being gathered up by the expanding blast and v is the expansion velocity. We can write that mass as

$$m = \rho\pi r^2 L, \tag{1.11}$$

where the length L is a constant assuming a cylindrical expansion, ρ is the mass density of the medium and r is the radius of the blast wave. Thus the energy is

$$E = \frac{1}{2}\rho\pi r^2 L v^2, \tag{1.12}$$

from which we can derive

$$v = \sqrt{\frac{2\varepsilon_L}{\rho\pi}} r^{-1}, \tag{1.13}$$

where $\varepsilon_L = E/L$ is the linear energy density. This can be also written as

$$\frac{dr}{dt} = \sqrt{\frac{2\varepsilon_L}{\rho\pi}} r^{-1}, \tag{1.14}$$

which, through direct integration yields

$$\frac{1}{2}r^2 = \sqrt{\frac{2\varepsilon_L}{\rho\pi}} t, \tag{1.15}$$

from which we can derive that

$$\varepsilon_L = \frac{1}{8}\rho\pi r^4 t^{-2}. \tag{1.16}$$

In conclusion, the shockwave front r as a function of time t scales as

$$r \propto t^{1/2}. \tag{1.17}$$

Sedov-Taylor model in 1D expansion

In exactly the same fashion, we can derive a relation of the shockwave front, radius r in one dimension. This time assuming a longitudinal expansion, the mass is

$$m = 2\rho r A, \tag{1.18}$$

where A is a constant area. Following the same steps, we can arrive at,

$$\varepsilon_A = \frac{4}{9}\rho r^3 t^{-2}, \tag{1.19}$$

where $\varepsilon_A = E/A$ is the surface energy density and

$$r \propto t^{2/3}. \tag{1.20}$$

To sum it up, based on the ST model for a 3D [53] to 1D expansion, we can write the shockwave front radius as a function of time as

$$\text{3D}: \quad E \propto \rho r^5 t^{-2} \quad \rightarrow \quad r \propto t^{2/5} \tag{1.21}$$

$$\text{2D}: \quad \varepsilon_L \propto \rho r^4 t^{-2} \quad \rightarrow \quad r \propto t^{2/4} \tag{1.22}$$

$$\text{1D}: \quad \varepsilon_A \propto \rho r^3 t^{-2} \quad \rightarrow \quad r \propto t^{2/3} \tag{1.23}$$

1.6.2 The free expansion regime

The derivation of the ST model assumes that the expanding blast wave is initially massless, *i.e.* that the only relevant mass is the mass it gathers up during the expansion. Early in the expansion, this is obviously a bad approximation, as the initial mass of the ablated material is dominant. It also results in an obviously unphysical behavior; the initial expansion velocity is infinitely large. Therefore, we look for an alternative derivation that takes into account the initial mass. In plasma physics and in the physics of supernova, this case is referred to as the free expansion regime. We will now discuss this regime in three, two and one dimension.

Free expansion model in 3D expansion

In analogy with the derivation of the ST scaling laws, we start by writing down the mass as a function of the radius r of the blast wave. In contrast to the ST case, we take into account the initial mass m_0 of the ablation plume. This yields

$$m = m_0 + \frac{4\pi}{3}\rho(r^3 - r_0^3), \tag{1.24}$$

where ρ is again the mass density of the surrounding atmosphere and r_0 is the initial radius of the blast wave. As before, we assume that all available energy is converted to kinetic energy and write

$$E = \frac{1}{2}mv^2 = \frac{1}{2}\left(m_0 + \frac{4\pi}{3}\rho(r^3 - r_0^3)\right)v^2, \tag{1.25}$$

which we solve for v to find the following differential equation

$$\frac{dr}{dt} = v = \sqrt{\frac{2E}{m_0 + \frac{4\pi}{3}\rho(r^3 - r_0^3)}}. \tag{1.26}$$

This differential equation can be easily solved numerically, but it is instructive to first consider some limiting cases. Specifically, we will look at what happens

at early times. In this case $r \approx r_0$ and as a result $\frac{4\pi}{3}\rho(r^3 - r_0^3) \ll m_0$, or in other words, the mass gathered up by the expansion is small compared to the initial mass. The radius r to which this holds obviously depends on the mass density ρ of the atmosphere. In this limit, the right hand side of the differential equation becomes constant and we find that the expansion velocity becomes

$$v_0 = \sqrt{\frac{2E}{m_0}}. \tag{1.27}$$

Using this definition, we can rewrite the above differential equation as

$$\frac{dr}{dt} = \frac{v_0}{\sqrt{1 + \frac{4\pi\rho}{3m_0}(r^3 - r_0^3)}}. \tag{1.28}$$

If we introduce an effective volume $V_{\text{eff}} = m_0/\rho$, which is a volume of surrounding atmosphere with the same mass as the initial mass and if we write this effective volume in terms of an effective radius r_{eff}, we find

$$\frac{dr}{dt} = \frac{v_0}{\sqrt{1 + (r^3 - r_0^3)/r_{\text{eff}}^3}}. \tag{1.29}$$

Numerically integrating this equation for typical initial condition ($v_0 = 5\,\text{km/s}$, $r_0 = 1\ \mu\text{m}$, $r_{\text{eff}} \approx 9.3\ \mu\text{m}$), yields the orange line in Fig. 1.7. To compare this result to the ST scaling law, we can use two approaches. The simplest approach is to compute the total energy $\frac{1}{2}m_0v_0^2$ and plot the resulting $r(t)$ according to the three-dimensional ST model [53]. This approach is illustrated as the blue line in Fig. 1.7. Alternatively, and perhaps experimentally more relevant, we can fit the long time behavior of the free expansion result with the ST scaling law and extract the energy from that fit. In order to find a proper fit, we have to allow for an initial radius. As can be seen in the green curve in Fig. 1.7, the fit yields a negative value for the initial radius. More interestingly, for these initial conditions, it turns out that the energy retrieved from the fit is roughly 80% higher than the actual initial energy.

Free expansion model in 2D expansion

Following the approach we used above, we find that in two dimensions, the differential equation describing the cylindrical blast wave expansion becomes

$$\frac{dr}{dt} = \frac{v_0}{\sqrt{1 + (r^2 - r_0^2)/r_{\text{eff}}^2}}, \tag{1.30}$$

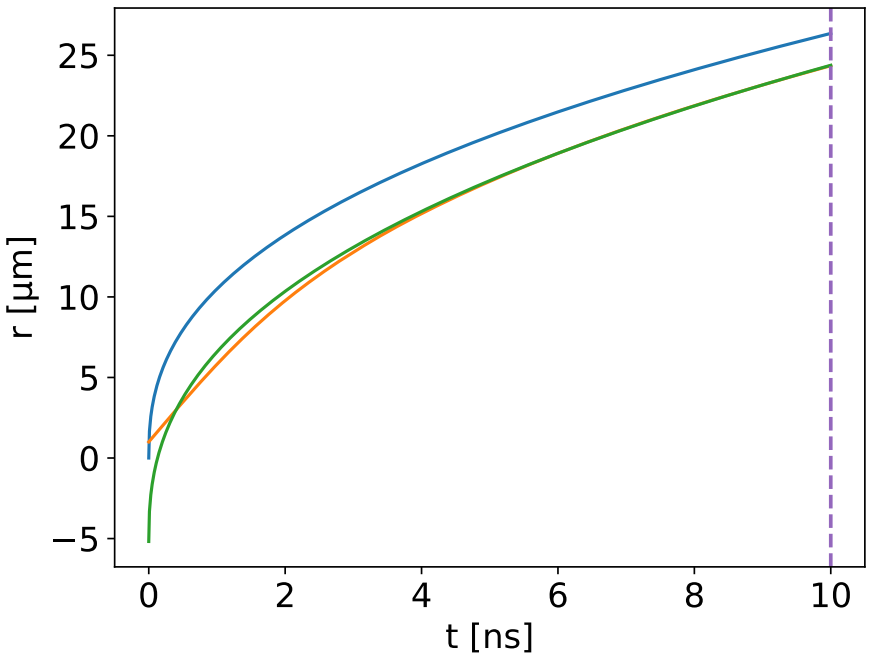

Figure 1.7: The free expansion model in 3D. The free expansion model in 3D (orange) and the Sedov-Taylor model in 3D (blue) as a function of the plume expansion time are shown. The green line is a long time behavior of the free expansion result fitted with the Sedov-Taylor model in 3D. The dashed line represents the experimentally relevant plume expansion time.

where r_{eff} has in this case been defined such that $V_{\text{eff}} = \pi L r_{\text{eff}}^2$, with L the same constant length as in Eq. 1.11. We numerically integrate this equation for the same initial conditions as we used in the three dimensional case and compare with the two-dimensional ST law. The result of this calculation is shown in Fig. 1.8, with the colors of the lines as they were used before. We see again that the ST law predicts a much larger expansion for the same linear energy density ε_L. If we fit the two dimensional free expansion result with the two dimensional ST law, we find that the ST fit requires a negative initial radius and yields a roughly 85% higher linear energy density.

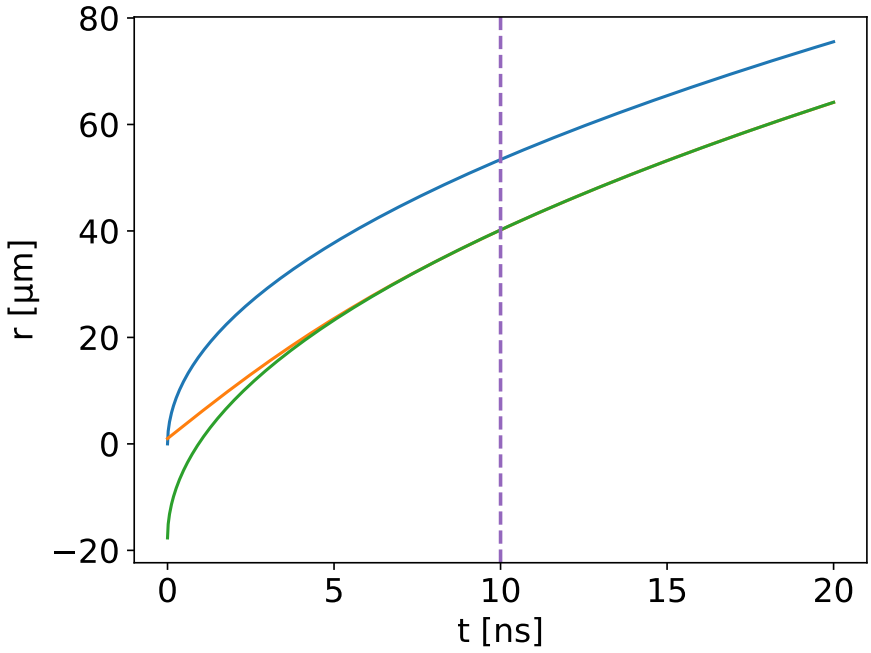

Figure 1.8: The free expansion model in 2D. The same colors denote the same lines as in Fig. 1.7.

Free expansion model in 1D expansion

Finally, we can follow the same procedure for the one dimensional case. The differential equation, predictably, becomes

$$\frac{dr}{dt} = \frac{v_0}{\sqrt{1 + (r - r_0)/r_{\text{eff}}}}, \tag{1.31}$$

where r_{eff} is defined such that $V_{\text{eff}} = 2rA$, in accordance with Eq. 1.18. The results of the numerical integration and the comparison with the relevant ST law is shown in Fig. 1.9. As before, the ST law deviates significantly from the numerical result.

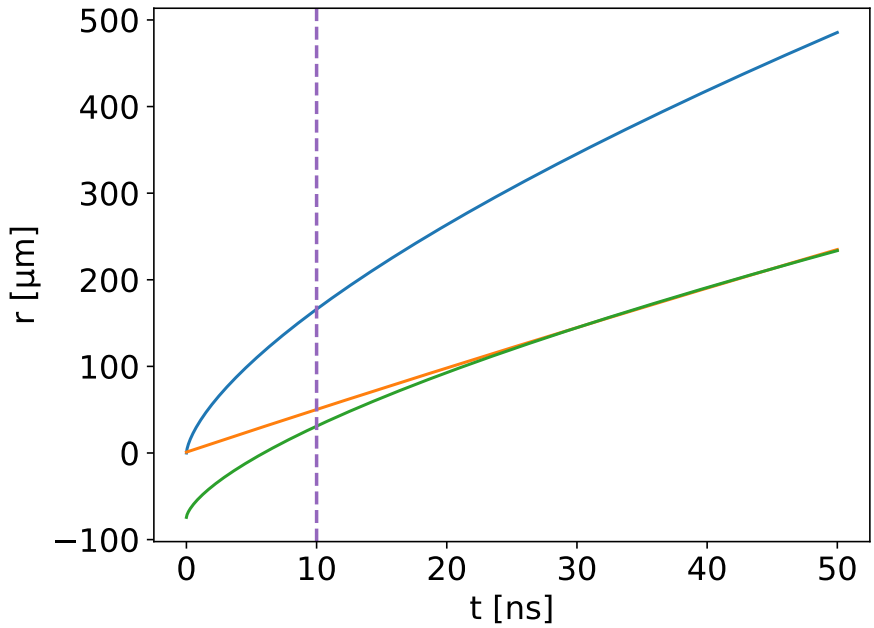

Figure 1.9: The free expansion model in 1D. The same colors denote the same lines as in Fig. 1.7.

It is important to note that the discrepancy between the ST result and the free expansion result is larger for lower dimensions. This can be easily understood as follows. When r becomes very large, the effect of the initial mass becomes smaller, as the mass that has been gathered up by the blast wave becomes much larger than the initial mass. For higher dimensions, mass is gathered up faster as a function of radius, which means that the system starts to follow a ST-like behavior already for smaller radii. The initial expansion of the ablation plume is highly supersonic and therefore mostly one dimensional, *i.e.* perpendicular to the surface. This means that the volume of superheated material, which starts out as an extremely flat disk, will rapidly get thicker. An interesting question then becomes: does the ablation plume change aspect ratio during its expansion? This obviously depends on the initial radius of the

plume and on its final height. We can use this as a criterion to distinguish between weak and strong focusing. In the case of weak focusing, the expansion runs out of steam before the aspect ratio changes. The expansion therefore tends to transition into an isotropic, ST-like expansion. We can define strong focusing as the situation in which this does not occur during the time scale that is being investigated.

In the following two Chapters, we will assume that we are in the strong focusing regime, *i.e.* that the expansion is dominated by the vertical component throughout the experiment. To verify this requires side-imaging, which is unfeasible as discussed before. The following two Chapters essentially describe the methods to learn more about the expansion dynamics without directly observing the vertical expansion.

Bibliography

[1] G. Mourou, "Nobel Lecture: Extreme light physics and application," Rev. Mod. Phys. **91**, 030501 (2019).

[2] F. Calegari, G. Sansone, S. Stagira, C. Vozzi, and M. Nisoli, "Advances in attosecond science," J. Phys. B. **49**, 062001 (2016).

[3] P. M. Paul, E. S. Toma, P. Breger, G. Mullot, F. Augé, P. Balcou, H. G. Muller, and P. Agostini, "Observation of a Train of Attosecond Pulses from High Harmonic Generation," Science **292**, 1689–1692 (2001).

[4] M. Schultze, M. Fieß, N. Karpowicz, J. Gagnon, M. Korbman, M. Hofstetter, S. Neppl, A. L. Cavalieri, Y. Komninos, T. Mercouris, C. A. Nicolaides, R. Pazourek, S. Nagele, J. Feist, J. Burgdörfer, A. M. Azzeer, R. Ernstorfer, R. Kienberger, U. Kleineberg, E. Goulielmakis, F. Krausz, and V. S. Yakovlev, "Delay in Photoemission," Science **328**, 1658–1662 (2010).

[5] K. Klünder, J. M. Dahlström, M. Gisselbrecht, T. Fordell, M. Swoboda, D. Guénot, P. Johnsson, J. Caillat, J. Mauritsson, A. Maquet, R. Taïeb, and A. L'Huillier, "Probing Single-Photon Ionization on the Attosecond Time Scale," Phys. Rev. Lett. **106**, 143002 (2011).

[6] M. Uiberacker, T. Uphues, M. Schultze, A. J. Verhoef, V. Yakovlev, M. F. Kling, J. Rauschenberger, N. M. Kabachnik, H. Schrder, M. Lezius, K. L. Kompa, H.-G. Muller, M. J. J. Vrakking, S. Hendel, U. Kleineberg, U. Heinzmann, M. Drescher, and F. Krausz, "Attosecond real-time observation of electron tunnelling in atoms," Nature **446**, 627–632 (2007).

[7] G. Sansone, L. Poletto, and M. Nisoli, "High-energy attosecond light sources," Nat. Photonics **5**, 655–663 (2011).

[8] S. Preuss, A. Demchuk, and M. Stuke, "Sub-picosecond UV laser ablation of metals," Appl. Phys. A **61**, 33–37 (1995).

[9] M. Feuerhake, J.-H. Klein-Wiele, G. Marowsky, and P. Simon, "Dynamic ablation studies of sub-micron gratings on metals with sub-picosecond time resolution," Appl. Phys. A **67**, 603–606 (1998).

[10] M. Li, K. Mori, M. Ishizuka, X. Liu, Y. Sugimoto, N. Ikeda, and K. Asakawa, "Photonic bandpass filter for 1550 nm fabricated by femtosecond direct laser ablation," Appl. Phys. Lett. **83**, 216–218 (2003).

[11] D. J. Hwang, C. P. Grigoropoulos, and T. Y. Choi, "Efficiency of silicon micromachining by femtosecond laser pulses in ambient air," J. Appl. Phys. **99**, 083101 (2006).

[12] P. Balling and J. Schou, "Femtosecond-laser ablation dynamics of dielectrics: basics and applications for thin films," Rep. Prog. Phys. **76**, 036502 (2013).

[13] A. Vogel and V. Venugopalan, "Mechanisms of Pulsed Laser Ablation of Biological Tissues," Chem. Rev. **103**, 577–644 (2003). PMID: 12580643.

[14] B. Rethfeld, K. Sokolowski-Tinten, D. von der Linde, and S. Anisimov, "Timescales in the response of materials to femtosecond laser excitation," Appl. Phys. A **79**, 767–769 (2004).

[15] D. von der Linde, K. Sokolowski-Tinten, and J. Bialkowski, "Lasersolid interaction in the femtosecond time regime," Appl. Surf. Sci. **109-110**, 1–10 (1997).

[16] B. Rethfeld, "Free-electron generation in laser-irradiated dielectrics," Phys. Rev. B **73**, 035101 (2006).

[17] K. Sokolowski-Tinten and D. von der Linde, "Generation of dense electronhole plasmas in silicon," Phys. Rev. B **61**, 2643–2650 (2000).

[18] B. Strycker, M. Springer, A. Traverso, A. Kolomenskii, G. Kattawar, and A. Sokolov, "Femtosecond-laser-induced shockwaves in water generated at an air-water interface," Opt. Express **21**, 23772–23784 (2013).

[19] S. Besner, J.-Y. Degorce, A. Kabashin, and M. Meunier, "Influence of ambient medium on femtosecond laser processing of silicon," Appl. Surf. Sci. **247**, 163–168 (2005).

[20] D. A. Willis and X. Xu, "Transport Phenomena and Droplet Formation During Pulsed Laser Interaction With Thin Films," Journal of Heat Transfer **122**, 763–770 (2000).

[21] X. Zeng, X. Mao, S. S. Mao, S.-B. Wen, R. Greif, and R. E. Russo, "Laser-induced shockwave propagation from ablation in a cavity," Appl. Phys. Lett. **88**, 61502 (2006).

[22] A. Vogel, S. Busch, and U. Parlitz, "Shock wave emission and cavitation bubble generation by picosecond and nanosecond optical breakdown in water," J. Acoust. Soc. Am. **100**, 148–165 (1996).

[23] C. Sarpe-Tudoran, A. Assion, M. Wollenhaupt, M. Winter, and T. Baumert, "Plasma dynamics of water breakdown at a water surface induced by femtosecond laser pulses," Appl. Phys. Lett. **88**, 261109 (2006).

[24] A. Vogel, J. Noack, G. Hüttman, and G. Paltauf, "Mechanisms of femtosecond laser nanosurgery of cells and tissues," Appl. Phys. B **81**, 1015–1047 (2005).

[25] J. v. Borkulo, P. Verburg, and R. v. d. Stam, "Multi Beam Full Cut Dicing of Thin Si IC Wafers," in "2017 IEEE 67th Electronic Components and Technology Conference (ECTC)," (2017), pp. 1817–1822.

[26] C. B. Schaffer, N. Nishimura, E. N. Glezer, A. M.-T. Kim, and E. Mazur, "Dynamics of femtosecond laser-induced breakdown in water from femtoseconds to microseconds," Opt. Express **10**, 196–203 (2002).

[27] K. Sokolowski-Tinten, J. Bialkowski, A. Cavalleri, D. von der Linde, A. Oparin, J. Meyer-ter Vehn, and S. I. Anisimov, "Transient States of Matter during Short Pulse Laser Ablation," Phys. Rev. Lett. **81**, 224–227 (1998).

[28] J. Hernandez-Rueda, D. Puerto, J. Siegel, M. Galvan-Sosa, and J. Solis, "Plasma dynamics and structural modifications induced by femtosecond laser pulses in quartz," Appl. Surf. Sci. **258**, 9389–9393 (2012).

[29] J. Hernandez-Rueda, J. Siegel, M. Galvan-Sosa, A. R. de la Cruz, M. Garcia-Lechuga, and J. Solis, "Controlling ablation mechanisms in sapphire by tuning the temporal shape of femtosecond laser pulses," J. Opt. Soc. Am. B **32**, 150–156 (2015).

[30] J. Hernandez-Rueda and D. van Oosten, "Dynamics of Ultrafast Laser Ablation of Water," arXiv preprint arXiv:1810.06946 (2018).

[31] J. Hernandez-Rueda and D. van Oosten, "Transient scattering effects and electron plasma dynamics during ultrafast laser ablation of water," Opt. Lett. **44**, 1856–1859 (2019).

[32] H. Zhang, D. M. Krol, J. I. Dijkhuis, and D. van Oosten, "Self-scattering effects in femtosecond laser nanoablation," Opt. Lett. **38**, 5032–5035 (2013).

[33] H. Zhang, S. A. Wolbers, D. M. Krol, J. I. Dijkhuis, and D. van Oosten, "Modeling and experiments of self-reflectivity under femtosecond ablation conditions," J. Opt. Soc. Am. B **32**, 606–616 (2015).

[34] B. H. Christensen and P. Balling, "Modeling ultrashort-pulse laser ablation of dielectric materials," Phys. Rev. B **79**, 155424 (2009).

[35] H. Zhang, "Single-shot femtosecond laser ablation on the nanoscale," Ph.D. thesis, Utrecht University (2013).

[36] T. T. P. Nguyen, R. Tanabe, and Y. Ito, "Comparative study of the expansion dynamics of laser-driven plasma and shock wave in in-air and underwater ablation regimes," Optics & Laser Technology **100**, 21–26 (2018).

[37] H. Rubinsztein-Dunlop, A. Forbes, M. V. Berry, M. R. Dennis, D. L. Andrews, M. Mansuripur, C. Denz, C. Alpmann, P. Banzer, T. Bauer, E. Karimi, L. Marrucci, M. Padgett, M. Ritsch-Marte, N. M. Litchinitser, N. P. Bigelow, C. Rosales-Guzmán, A. Belmonte, J. P. Torres, T. W. Neely, M. Baker, R. Gordon, A. B. Stilgoe, J. Romero, A. G. White, R. Fickler, A. E. Willner, G. Xie, B. McMorran, and A. M. Weiner, "Roadmap on structured light," J. Opt. **19**, 013001 (2016).

[38] F. M. Dickey, *Laser Beam Shaping* (CRC Press, 2014), 2nd ed.

[39] G. Lazarev, P.-J. Chen, J. Strauss, N. Fontaine, and A. Forbes, "Beyond the display: phase-only liquid crystal on Silicon devices and their applications in photonics [Invited]," Opt. Express **27**, 16206–16249 (2019).

[40] H. Tamura, T. Unakami, J. He, Y. Miyamoto, and K. Nakagawa, "Highly uniform holographic microtrap arrays for single atom trapping using a feedback optimization of in-trap fluorescence measurements," Opt. Express **24**, 8132–8141 (2016).

[41] F. Nogrette, H. Labuhn, S. Ravets, D. Barredo, L. Béguin, A. Vernier, T. Lahaye, and A. Browaeys, "Single-Atom Trapping in Holographic 2D Arrays of Microtraps with Arbitrary Geometries," Phys. Rev. X **4**, 021034 (2014).

[42] A. L. Gaunt and Z. Hadzibabic, "Robust Digital Holography For Ultracold Atom Trapping," Sci. Rep. **2**, 721 (2012).

[43] M. Padgett and R. Di Leonardo, "Holographic optical tweezers and their relevance to lab on chip devices," Lab Chip **11**, 1196–1205 (2011).

[44] E. R. Dufresne, G. C. Spalding, M. T. Dearing, S. A. Sheets, and D. G. Grier, "Computer-generated holographic optical tweezer arrays," Review of Scientific Instruments **72**, 1810–1816 (2001).

[45] C. Zhang, Y. Hu, W. Du, P. Wu, S. Rao, Z. Cai, Z. Lao, B. Xu, J. Ni, J. Li, G. Zhao, D. Wu, J. Chu, and K. Sugioka, "Optimized holographic femtosecond laser patterning method towards rapid integration of high-quality functional devices in microchannels," Sci. Rep. **6**, 33281 (2016).

[46] L. Durdevic, H. M. L. Robert, B. Wattellier, S. Monneret, and G. Baffou, "Microscale Temperature Shaping Using Spatial Light Modulation on Gold Nanoparticles," Sci. Rep. **9**, 4644 (2019).

[47] A. P. Mosk, A. Lagendijk, G. Lerosey, and M. Fink, "Controlling waves in space and time for imaging and focusing in complex media," Nat. Photonics **6**, 283–292 (2012).

[48] P. S. Salter and M. J. Booth, "Adaptive optics in laser processing," Light Sci. Appl. **8**, 110 (2019).

[49] A. A. Kuchmizhak, A. P. Porfirev, S. A. Syubaev, P. A. Danilov, A. A. Ionin, O. B. Vitrik, Y. N. Kulchin, S. N. Khonina, and S. I. Kudryashov, "Multi-beam pulsed-laser patterning of plasmonic films using broadband diffractive optical elements," Opt. Lett. **42**, 2838–2841 (2017).

[50] D. Pavlov, S. Gurbatov, S. I. Kudryashov, P. A. Danilov, A. P. Porfirev, S. N. Khonina, O. B. Vitrik, S. A. Kulinich, M. Lapine, and A. A. Kuchmizhak, "10-million-elements-per-second printing of infrared-resonant plasmonic arrays by multiplexed laser pulses," Opt. Lett. **44**, 283–286 (2019).

[51] A. Mohl, S. Kaldun, C. Kunz, F. A. Muller, U. Fuchs, and S. Graf, "Tailored focal beam shaping and its application in laser material processing," J. Laser Appl. **31**, 042019 (2019).

[52] T. Hafner, J. Strauß, C. Roider, J. Heberle, and M. Schmidt, "Tailored laser beam shaping for efficient and accurate microstructuring," Appl. Phys. A **124**, 111 (2018).

[53] L. I. Sedov, *Similarity and Dimensional Methods in Mechanics* (CRC press, 1993).

[54] S. P. Reynolds, "Supernova Remnants at High Energy," Annu. Rev. Astron. and Astrophys. **46**, 89–126 (2008).

[55] M. Pasienski and B. DeMarco, "A high-accuracy algorithm for designing arbitrary holographic atom traps," Opt. Express **16**, 2176–2190 (2008).

2 An optical method for micron-scale tracer-less visualization of ultra-fast laser induced gas flow at a water/air interface

Abstract. We study femtosecond laser-induced flows of air at a water/air interface, at micrometer length scales. To visualize the flow velocity field, we simultaneously induce two flow fronts using two adjacent laser pump spots. Where the flows meet, a stationary shockwave is produced, the length of which is a measure of the local flow velocity at a given radial position. By changing the distance between the spots using a spatial light modulator, we map out the flow velocity around the pump spots. We find gas front velocities near the speed of sound in air v_s for two laser excitation energies. We find an energy scaling that is inconsistent with the Sedov-Taylor model.[1]

2.1 Introduction

Laser ablation is currently applied in research fields ranging from life-science to laser materials processing [1–4]. In particular, the use of femtosecond laser pulses is very appealing to induce ablation, mainly due to the ultrafast laser energy deposition and the extreme non-linearity of the process [5–8]. These

[1] This chapter is based on "An optical method for micron-scale tracer-less visualization of ultra-fast laser induced gas flow at a water/air interface", Dashdeleg Baasanjav, Javier Hernandez-Rueda, Allard P. Mosk, and Dries van Oosten, accepted for publication in Applied Optics. D. B. and J. H. R. contributed equally to the experimental work presented in this chapter. D. B. carried out the data analysis and calculation. All authors contributed to the interpretation.

mechanisms have very distinct advantages, such as significantly reducing the heat-related collateral effects and achieving a sub-diffraction limit spatial resolution [7]. Besides these technical advantages, the ultrafast nature of the laser excitation leads to a concatenation of several processes that are spread over different time-scales, which is especially interesting to compartmentalize the problem. On the time-scale of the order of the pulse duration, the laser energy is absorbed and a hot electron plasma is created. Depending on the photon energy and the electronic properties of the target, the absorption process can be mostly non-linear (*i.e.* dielectrics, semiconductors) or linear (*i.e.* semiconductors, metals). For water (a dielectric) the initial absorption is due to multiphoton ionization, and therefore non-linear. However, the excited electrons also induce linear absorption, through inverse bremsstrahlung and impact ionization [9, 10]. On the picosecond time-scale, the electrons thermalize with the atoms and molecules, which can lead to a phase change. In the specific example of water, this leads to the production of a volume of strongly supercritical water. This volume will then rapidly expand, subjecting the target underneath to a strong recoil pressure, leading to liquid flow and potentially to splashing, on the microsecond time-scale. To understand this liquid flow, it is of course paramount to know the initial thermodynamic conditions. To determine these initial conditions, the dynamics of the ablation plume expanding into the background gas needs to be fully understood. The dynamics during ultrafast ablation of liquids have been investigated using a number of time-resolved imaging methods, providing a wealth of information on the expansion of the plume [9–20]. However, the flow velocity of the gas that surrounds the expanding plasma cannot be directly visualized, as the length scales are far too small for traditional methods using tracer particles and the available time-resolved imaging techniques cannot resolve the subtle changes on the refractive index of the gas flow on the micrometer scale.

We recently reported on the generation and visualization of shockwaves at a water/air interface using multiple excitation spots in close proximity [21]. The resulting (opposing) gas flows produced at each irradiation spot can have a relative velocity exceeding the speed of sound, resulting in stationary shocks. These shocks give significant optical contrast in a reflectivity measurement, because they extend along the line of sight, as illustrated in Fig. 2.1. In this chapter, we demonstrate the use of a spatial light modulator to change the distance between the excitation spots on-the-fly. We use this method to investigate the radial dependence of the gas flow velocity around the excitation

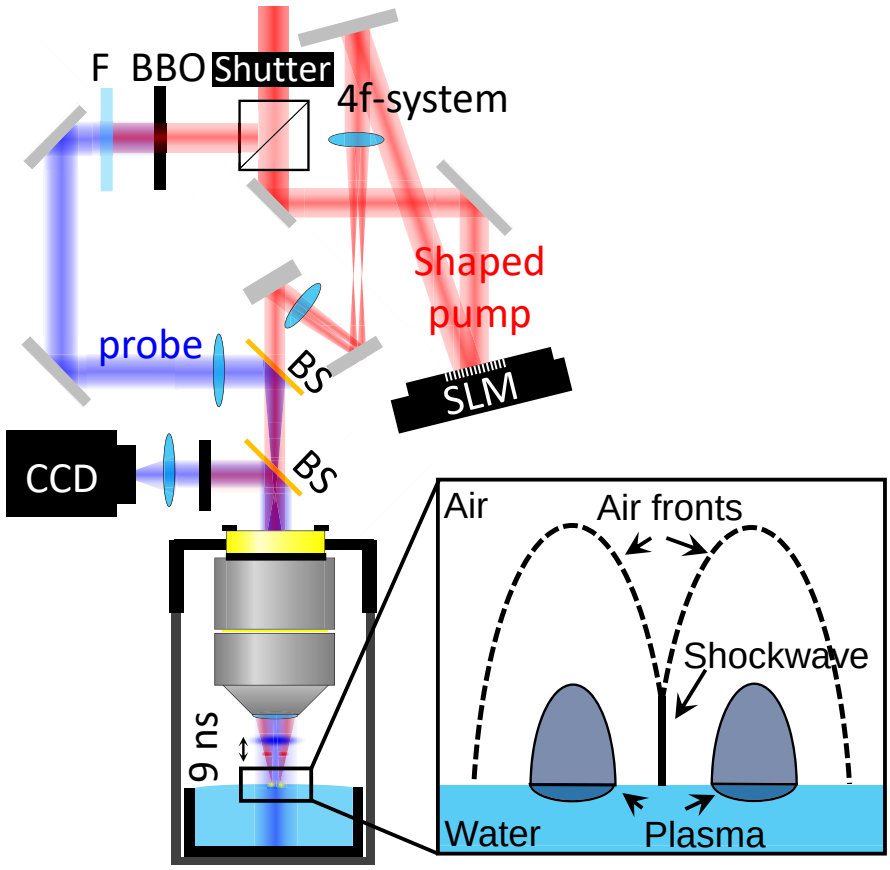

Figure 2.1: Illustration of the experimental setup. Light from an amplified femtosecond laser is split into two paths. One path (pump, in red) is reflected on a spatial light modulator (SLM), shaping the phase of the beam. The surface of the SLM is imaged in the back focal plane of a microscope objective. The other path (probe, in blue) is first frequency doubled and focused in the back focal plane of the same microscope objective, leading to wide-field illumination. The pump-probe delay is set using a delay line in the probe path. The inset illustrates the geometry of the laser-excited water surface using a double pump.

spots. We determine the local flow velocity by measuring the length of the resulting shockwaves and discuss energy dependence of the flow velocity field. Finally, we discuss future application of our method.

2.2 Experimental setup

In Fig. 2.1, we show a diagram of the setup. Laser pulses from an amplified femtosecond laser (Hurricane, Spectra-Physics), with a duration of 150 fs and a wavelength of 800 nm are first split into a probe and a pump path using a polarizing beam splitter (PBS). For the experiments, we use a single laser shot that is picked using a mechanical shutter. The probe pulse is frequency doubled using a beta barium borate (BBO) crystal. Subsequently, the probe beam is focused in the back focal plane of a microscope objective to achieve wide field illumination. The pump beam is reflected on a spatial light modulator (SLM, Holoeye Pluto-BB for 700-1000nm), which is used to imprint a phase pattern on the beam. This phase pattern is imaged in the back focal plane of the objective using two lenses in a 4-f arrangement. We use phase maps of binary gratings that result in two dominant ($\pm 1^{st}$) diffraction orders, resulting in two adjacent spots on the sample surface. By varying the period of the grating, we can vary the separation between the spots.

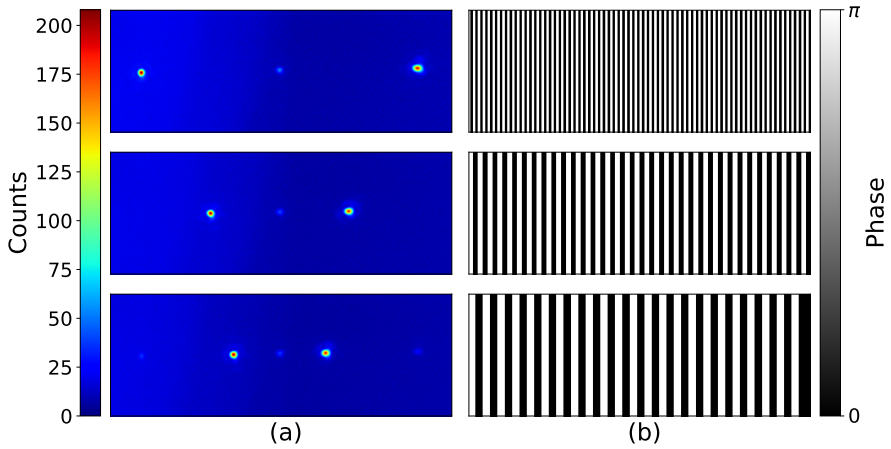

Figure 2.2: (a) Typical intensity patterns achieved in an intermediate image plane. (b) Corresponding binary gratings displayed on the SLM.

As a proof of principle, Fig. 2.2(a) shows typical illumination patterns

recorded at the Fourier plane of the 4-f system with highly attenuated fs laser pulses. Fig. 2.2(b) shows the corresponding grating patterns displayed on the SLM. In all illumination patterns, a small amount of light can be seen in the center, corresponding to the zeroth order (specular) reflection of the SLM. Also, in the bottom image, weak higher order spots can be seen. As long as these spots are sufficiently below the ablation threshold, they do not affect the measurements. The illumination patterns shown in Fig. 2.2(a) are imaged onto the surface of a sample that consists of 25 mL of milli-Q demineralized water. The light reflected from the surface is collected by the objective. The reflected pump light is blocked by a bandpass filter (400±10 nm). The reflected probe light is used to image the laser-excited water/air interface, by means of a tube lens (TL). The image is recorded using an electron multiplying CCD camera (Andor, Ixon 885). In all experiments describe in the work, we set the delay between the pump and the probe to 9 ns.

2.3 Transient-reflectivity measurement results

In Fig. 2.3, we display transient reflectivity images obtained during the double-spot ablation process using several grating periods. For all images, we observe two dark circles at the laser excited locations. We attribute these to the reduced reflectivity due to the expanding ablation plume that absorbs and scatters the probe-light. We also observe ring-like features concentrically around these spots. These appear to be related to shockwaves in the surrounding air. We verified this by replacing the air above the water surface with helium, in which the rings are absent, as shown in Section 1.2. Most interestingly, we observe a strong stationary shock in between the two spots. This shockwave is caused by the fact that the opposing air flows resulting from the adjacent spots have a relative velocity that is strongly supersonic. With decreasing distance between the spots, the length of this stationary shock changes. In Fig. 2.3(c), we see that the stationary shock has a small curvature. This can be attributed to a slight imbalance in the energy of the two pulses as systematically demonstrated elsewhere [21]. Such an imbalance can, for instance, be caused by a slight tilt of the water surface produced by small vibrations. To assess the imbalance, the radii of the black regions are computed for each image using a Hough transformation (HoughCircles, OpenCV), see red circumferences in Fig. 2.3(b).

For a given pulse energy, the average and standard deviation of all radii are

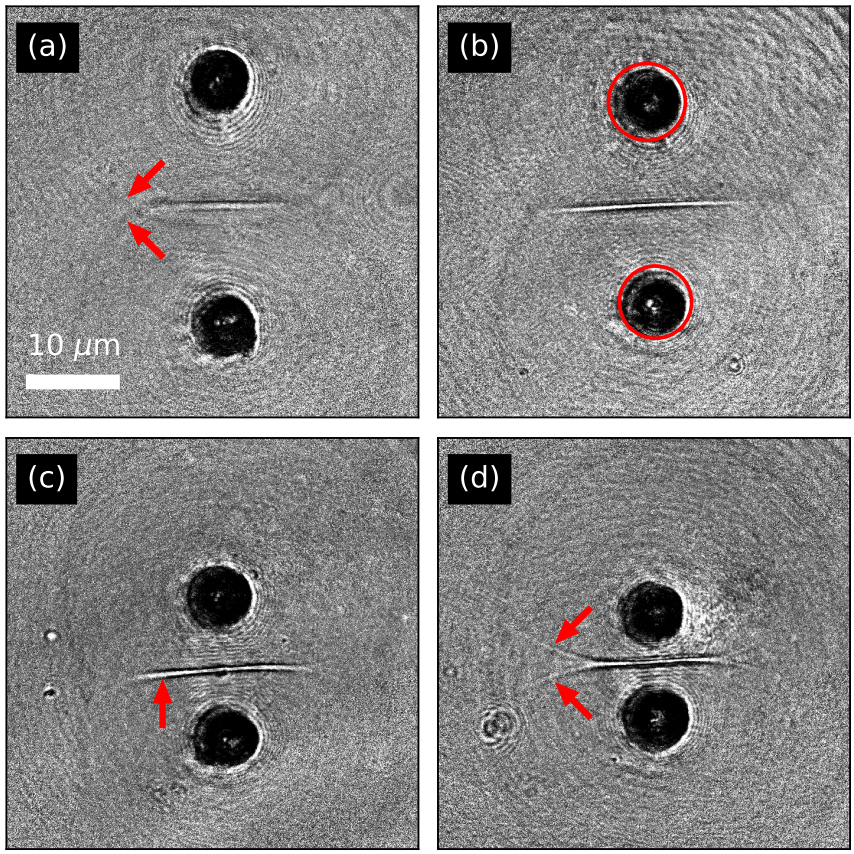

Figure 2.3: Transient reflectivity images obtained at a pump-probe delay of 9 ns and a fluence of 18 J/cm^2, for varying pump spot separation. The arrows in (a) points to weak shockwaves. The red circles in (b) illustrates the radius of the black regions as determined using a Hough transform. The arrows in (c) indicate the stationary shock caused by the opposing gas flow from the two excitation spots. The arrows in (d) show the bifurcation of the shockwave.

calculated. Images in which both radii are within one standard deviation of the average are used in the rest of the analysis. In Fig. 2.3(d), we see that the stationary shock bifurcates at both ends. We can understand this as follows. When the gas flow reaches the shockwave, the increased local pressure causes the flow to partly deflect sideways. In the case of Fig. 2.3(d), the vapor and the shockwave are so close together that this deflection leads to a significant flow velocity component parallel to the stationary shock. This parallel flow adds to the radial flow, causing the flow to significantly exceed the speed of sound, resulting in the bifurcating tails of the stationary shockwave.

2.4 Gas front velocity estimation

In Fig. 2.5(a), we plot the length L of the stationary shock as a function of d, where $2d$ is the distance between the centers of the excitation spots, for two peak-fluences (18 J/cm^2 and 21 J/cm^2) on the sample surface. In the measurement of the length, we take into account only the straight section, discarding the bifurcating tails if they occur (as is the case in Fig. 2.3(d)). The circled data points correspond to the images in Fig. 2.3 (the letter indicating the relevant subplot). We observe that as the distance between the pump spots is increased, the length of the shock grows until it reaches a maximum, after which it decreases again. This decrease can be attributed to the fact that at the pump-probe delay of 9 ns, the air flow is only just reaching the halfway point between the two excitation spots. The dashed vertical lines in the graph correspond to the distance at which we first observe the bifurcation of the shockwave. As can be seen, the occurrence of the bifurcation does not seem to significantly change the trend. Nevertheless, care should be taken when interpreting the results for shorter distances, as the bifurcation indicates a significant deflection of the flow.

As argued in [21], to observe these stationary shocks, the velocity from each excitation spot must be such that the component perpendicular ($v_\perp$) to the shock, shown in Fig. 2.4, is larger than half the velocity of sound ($v_s = 343$ m/s). In this way, the perpendicular components satisfy $v_\perp^{up} + v_\perp^{down} \geq v_s$. Therefore, the length L of the stationary shock is determined by the point where $v_\perp = v_s/2$. At this position, the perpendicular velocity can be written as $v_\perp = vd/r$, where $r = \sqrt{d^2 + (L/2)^2}$ and v is the radial flow velocity due to a single excitation spot. From this equation and the above criterion, we

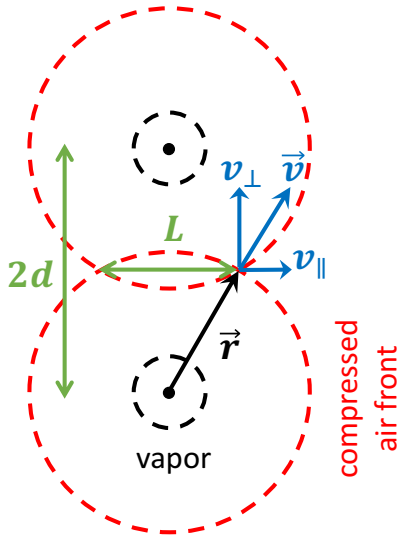

Figure 2.4: Geometrical scheme of the double pulse excitation.

find that

$$v = v_s \frac{\sqrt{4d^2 + L^2}}{d}. \tag{2.1}$$

This equation is used to convert the length into a radial velocity. The result of this conversion is shown in Fig. 2.5(b). For a spot separation of 14 μm ($d = 7\mu$m) and a fluence of 18 J/cm^2, we find a velocity of 280 ± 27 m/s. This value is in agreement with our previously reported results on the ultrafast laser ablation dynamics of water using double beam illumination at a single separation distance [21]. We see that, as expected, the radial velocity decreases as a function of the radial distance r. We also see that, surprisingly, the radial velocity seems almost independent of the incident pulse energy. Note that for large spot separations, the radius r seems to decrease again. This is a consequence of the fact that the length L decreases for large d. Beyond the maximum in L, the results plotted in Fig. 2.5(b) are therefore unreliable. The solid vertical lines in the graphs mark the average radius of the black regions in Fig. 2.5 and, as before, the dashed vertical lines correspond to the distance where we first observe bifurcation of the shock, indicating the point where deflection of the flow becomes important. For shorter distances, Eq. 2.1 therefore underestimates the local flow velocity.

The black circles in Fig. 2.5(b) are the data for 21 J/cm^2 but with r scaled

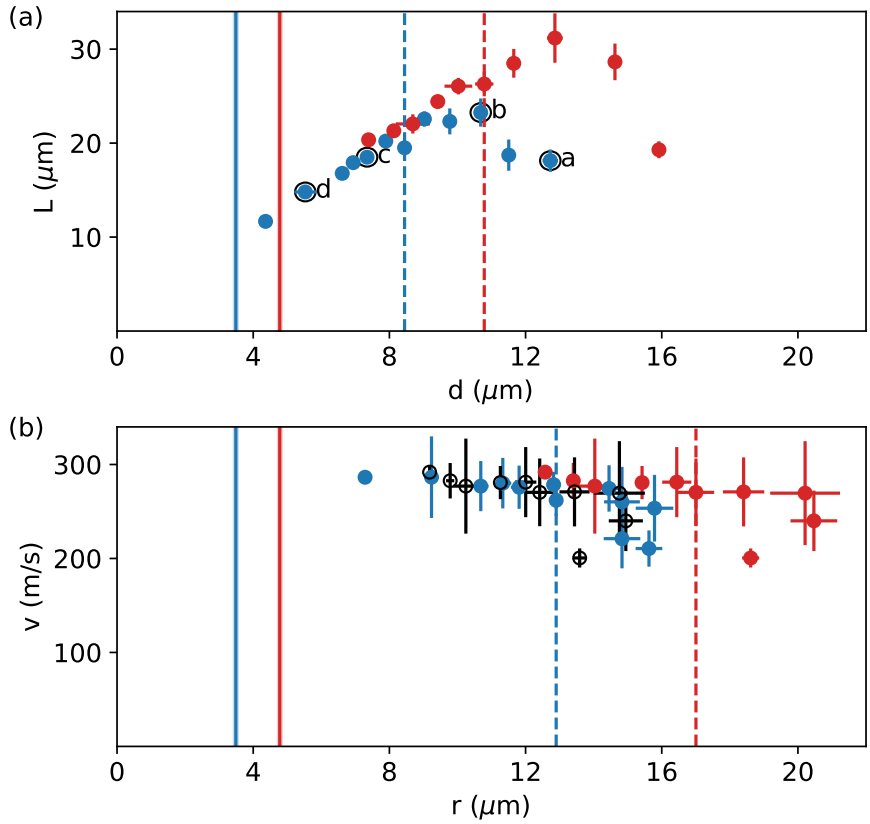

Figure 2.5: (a) Shockwave length as a function of distance d between pump and the shockwave, for 18 J/cm^2 (blue) and 21 J/cm^2 (red). The dashed vertical lines indicate the distance below which bifurcation of the stationary shock is observed. The circled data points correspond to the typical images in Fig. 2.3, the letter indicating the relevant subplot. (b) Corresponding velocity as a function of radial distance r. The solid vertical lines indicate the radius of the black disk in the images. The open black symbols are the data for 21 J/cm^2 with the scaled r-axis, such that the points best overlap with the data for 18 J/cm^2.

down by a factor 1.36±0.07 (corresponding to the ratio of the radii of the black regions for the two energies), leaving the velocity unscaled. The fact that the datasets for 18 J/cm^2 and 21 J/cm^2 (corresponding to E_1 = 3.4 μJ and E_2 = 4.0 μJ per spot, respectively) then collapse onto each other suggests an approximately quadratic scaling with incident energy (as $(E_2/E_1)^m \approx 1.37$ with $m = 1.9 \pm 0.3$). However, the relevant energy for the gas flow is the absorbed rather than the incident energy. We therefore need to take into account how the absorbed energy depends on the incident energy. In transparent materials, the light absorption is in first order mediated by multi-photon ionization and avalanche ionization, which scale with different powers of the incident laser intensity, I^n and I, respectively. If we consider only multi-photon absorption, the order of the process n is defined as the number of laser photons needed to overcome the ionization potential of water $U/\hbar\omega = 6$, where U = 9.5 eV and $\hbar\omega$ = 1.56 eV. We could thus assume that the absorbed energy E_{abs} scales as $E_{abs} \propto E^6$, with E the incident energy. However, this does not take into account the effect of avalanche ionization. Therefore, we run a full calculation of the deposited energy within the irradiated water volume by using a finite-difference time-domain algorithm combined with the multiple rate equations method (MRE), as we recently reported [9] and as briefly discussed in Section 1.3. From the simulation, we find that the ratio of absorbed energies, given the pulse energies used in the experiment, is ~ 1.29, whereas the ratio of the pulse energies is ~ 1.18. This suggests a scaling of $E_{abs} \propto E^n$, with $n \sim 1.5$, as opposed to the power 6 we naively assumed on the basis of the multi-photon ionization. Using this result, we find that the quadratic scaling in the incident energy corresponds to a scaling with the absorbed energy to the power of 1.3 ± 0.2, rather than the $E_{abs}^{1/3}$ scaling one might expect on the basis of the Sedov-Taylor solution for a three dimensional point blast model [22]. Obviously, a full study of the energy scaling behavior would require experiments at significantly more laser energies. Yet, these results already lay bare a) the obvious limitations of applying the Sedov-Taylor model to an expansion that is not necessarily self-similar and b) the need to account for both linear and non-linear excitation.

2.5 Conclusion and outlook

In summary, we demonstrate the use of a spatial light modulator to visualize the light-induced-flow velocity field during ultra-fast laser ablation. We have

reconstructed the fs-laser induced air flow velocity profile for two different excitation energies. We find that the flow velocity is almost independent of the laser pulse energy, but that the radial scale of the velocity field depends approximately quadratically on the laser pulse energy. By computing the absorbed energy as a function of the incident pulse energy, considering both non-linear and linear laser excitation using an MRE model, we show that such an energy scaling is incompatible with a Sedov-Taylor like behavior, illustrating the limitations of applying the Sedov-Taylor model in this context. The use of a spatial light modulator opens up the possibility of creating exotic illumination patterns that would lead to more complex effects. For instance, a toroidal excitation pattern would lead to converging gas flow on the liquid/gas interface. One can envision the use of such converging shockwaves to focus an ablation plume, which might have application in pulsed laser deposition. Furthermore, our method of flow visualisation using spatial light modulator can readily be applied in such illumination geometries.

Bibliography

[1] R. R. Gattass and E. Mazur, "Femtosecond laser micromachining in transparent materials," Nat. Photonics **2**, 219–225 (2008).

[2] U. K. Tirlapur and K. Knig, "Targeted transfection by femtosecond laser," Nature **418**, 290–291 (2002).

[3] Z. Nagy, A. Takacs, T. Filkorn, and M. Sarayba, "Initial Clinical Evaluation of an Intraocular Femtosecond Laser in Cataract Surgery," J. Refract. Surg. **25**, 1053–1060 (2009).

[4] J. Hernandez-Rueda, J. Siegel, M. Galvan-Sosa, A. R. de la Cruz, M. Garcia-Lechuga, and J. Solis, "Controlling ablation mechanisms in sapphire by tuning the temporal shape of femtosecond laser pulses," J. Opt. Soc. Am. B **32**, 150–156 (2015).

[5] B. Rethfeld, "Unified Model for the Free-Electron Avalanche in Laser-Irradiated Dielectrics," Phys. Rev. Lett. **92**, 187401 (2004).

[6] B. Rethfeld, "Free-electron generation in laser-irradiated dielectrics," Phys. Rev. B **73**, 035101 (2006).

[7] P. Balling and J. Schou, "Femtosecond-laser ablation dynamics of dielectrics: basics and applications for thin films," Rep. Prog. Phys. **76**, 036502 (2013).

[8] B. H. Christensen and P. Balling, "Modeling ultrashort-pulse laser ablation of dielectric materials," Phys. Rev. B **79**, 155424 (2009).

[9] J. Hernandez-Rueda and D. van Oosten, "Transient scattering effects and electron plasma dynamics during ultrafast laser ablation of water," Opt. Lett. **44**, 1856–1859 (2019).

[10] T. Winkler, C. Sarpe, N. Jelzow, L. L. H., N. Gtte, B. Zielinski, P. Balling, A. Senftleben, and T. Baumert, "Probing spatial properties of electronic excitation in water after interaction with temporally shaped femtosecond laser pulses: Experiments and simulations," Appl. Surf. Sci. **374**, 235–242 (2016). E-MRS 2015 Spring Meeting Symposium CC: Laser and plasma processing for advanced applications in material science, 11-15 May 2015, Lille (France).

[11] R. R. Krueger, J. S. Krasinski, C. Radzewicz, K. G. Stonecipher, and J. J. Rowsey, "Photography of shock waves during excimer laser ablation of the cornea: Effect of helium gas on propagation velocity," Cornea **12**, 330–334 (1993).

[12] T. Juhasz, X. H. Hu, L. Turi, and Z. Bor, "Dynamics of shock waves and cavitation bubbles generated by picosecond laser pulses in corneal tissue and water," Lasers Surg. Medicine **15**, 91–98 (1994).

[13] C. B. Schaffer, N. Nishimura, E. N. Glezer, A. M.-T. Kim, and E. Mazur, "Dynamics of femtosecond laser-induced breakdown in water from femtoseconds to microseconds," Opt. Express **10**, 196–203 (2002).

[14] A. Vogel and V. Venugopalan, "Mechanisms of Pulsed Laser Ablation of Biological Tissues," Chem. Rev. **103**, 577–644 (2003). PMID: 12580643.

[15] I. Apitz and A. Vogel, "Material ejection in nanosecond Er:YAG laser ablation of water, liver, and skin," Appl. Phys. A **81**, 329–338 (2005).

[16] C. Sarpe, J. Khler, T. Winkler, M. Wollenhaupt, and T. Baumert, "Real-time observation of transient electron density in water irradiated with tailored femtosecond laser pulses," New J. Phys. **14**, 075021 (2012).

[17] B. Strycker, M. Springer, A. Traverso, A. Kolomenskii, G. Kattawar, and A. Sokolov, "Femtosecond-laser-induced shockwaves in water generated at an air-water interface," Opt. Express **21**, 23772–23784 (2013).

[18] N. Linz, S. Freidank, X.-X. Liang, H. Vogelmann, T. Trickl, and A. Vogel, "Wavelength dependence of nanosecond infrared laser-induced breakdown in water: Evidence for multiphoton initiation via an intermediate state," Phys. Rev. B **91**, 134114 (2015).

[19] T. T. Nguyen, R. Tanabe, and Y. Ito, "Comparative study of the expansion dynamics of laser-driven plasma and shock wave in in-air and underwater ablation regimes," Opt. & Laser Technology **100**, 21–26 (2018).

[20] J. Hernandez-Rueda and D. van Oosten, "Dynamics of Ultrafast Laser Ablation of Water," arXiv preprint arXiv:1810.06946 (2018).

[21] M. Vreugdenhil, D. van Oosten, and J. Hernandez-Rueda, "Dynamics of femtosecond laser-induced shockwaves at a water/air interface using multiple excitation beams," Opt. Lett. **43**, 4899–4902 (2018).

[22] L. I. Sedov, *Similarity and Dimensional Methods in Mechanics* (CRC press, 1993).

3 Femtosecond laser-ablation of gel and water

Abstract. We study the expansion dynamics of super-heated material during ultra-fast laser ablation of water and gel, using transient-reflectivity microscopy. We find that the expansion dynamics of water and gel, as observed during the first few nanoseconds, are extremely similar over a large range of ablation energies. We measure the crater topography of the gel after irradiation with a single laser shot, using optical interferometric microscopy, and estimate the mass that is ejected during the ablation. We calculate the laser energy deposited during irradiation by simulating the precise spatial distribution of the electron plasma density and temperature. We link the amount of removed mass obtained experimentally with the simulations of the deposited laser energy.[1]

3.1 Introduction

The advent of femtosecond (fs) laser amplification has, over the last three decades, enabled the study of the interaction of extremely intense light fields with dielectric materials. Many of these studies focused on the use of the above-mentioned interaction to produce permanent material changes, which gave rise to the field of fs-laser micromachining of transparent materials [1–4], half way between the fields of photonics and materials science. Similarly, permanent fs-laser-induced changes have singularly important applications in the field of laser-based surgery, *i.e.* neurosurgery and ocular surgery [5–10]. A key problem in laser-tissue interactions is the so-called photomechanical damage that results of the conversion of light energy into mechanical energy [11–13].

[1]This chapter is based on "Femtosecond laser-ablation of gel and water", Javier Hernandez-Rueda, Dashdeleg Baasanjav, Allard P. Mosk, and Dries van Oosten, accepted for publication in Optics Letters. D. B. and J. H. R. contributed equally to the experimental work presented in this chapter. D. B. carried out the data analysis and calculation. All authors contributed to the interpretation.

Light-tissue interactions are very complicated to model and so understanding the physical mechanisms that mediate the interaction of intense ultrashort laser pulses with water is crucial, since water is the main constituent of biological tissue.

Laser-water interactions have extensively been studied, with nanosecond [14–16], picosecond [16, 17] and femtosecond laser pulses [18–22]. Here, it is of paramount importance to realize the different 1) laser energy absorption mechanisms and 2) the time-scales in which absorption occurs. For short (pico- to nanosecond) pulses the energy is absorbed mainly through the excitation of impurities in water and later on via avalanche ionization [23]. Once the laser creates a plasma it keeps supplying energy to that plasma up to several picoseconds or nanoseconds, which means that the super-heated material expands while the laser field is still present. For ultrashort laser pulses the energy absorption is mediated via strong field ionization (*i.e.* multiphoton and tunneling ionization) and avalanche ionization [24–27], similarly to the situation in a transparent solid target [28–33]. In this case, the energy deposition is ultrafast, which leads to a distinct separation in time of the energy deposition (< 1 ps) and the material expansion onset (50 ps-1 ns) [18, 22]. This separation helps to compartmentalize the problem. Recently, our group reported on a model that explains the laser-induced electron plasma properties in water during the first picosecond. The model simultaneously accounts for laser pulse propagation and nonlinear energy absorption considering a dynamically evolving dielectric function of excited water, which is validated using the experimentally acquired transient reflectively [27]. It therefore provides an estimate of the spatial distribution of the deposited energy. The expansion dynamics is also quite well studied (mainly for longer pulses as explained above), but information about ejected water mass is hard to obtain due to the lack of an aftermath.

In this chapter, we use single femtosecond laser pulses to investigate laser ablation of water and a porcine-based gel. Using time-resolved microscopy we link distinct features of the material expansion during the nanosecond timescale. This comparison enables us to establish a reasonable correspondence between the ultrafast laser ablation in gel and water. Furthermore, the use of the gel specimen has two clear benefits, it is a better tissue phantom than water is and it provides a measure of the ejected mass that is estimated by measuring the volume of the single-laser-shot-generated craters. We use model calculations [27], to estimate the energy that is deposited using different laser

fluences and compare it to the ejected mass.

3.2 Setup and gel preparation

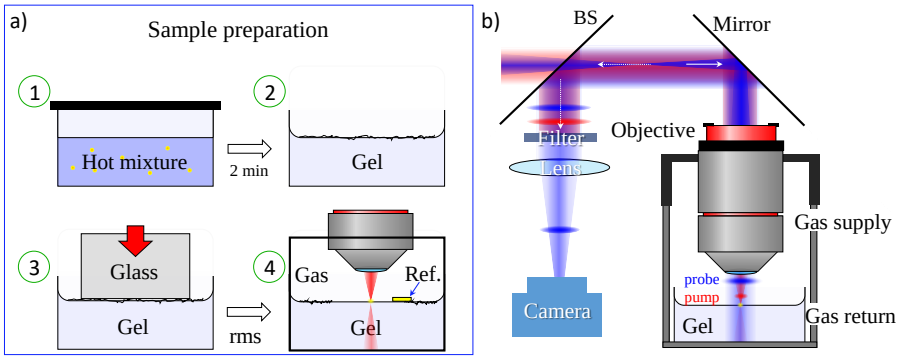

Figure 3.1: a) To prepare gel samples with a sufficiently flat surface, the gel is mixed (1) and allowed to partially set (2), after which an optical flat is gently dropped onto the surface (3). After the gel has fully set, the optical flat is removed and the sample is mounted in the ablation setup (4). b) The gel sample is mounted in a cuvette, such that the composition of the gas above the gel can be controlled. The gel is illuminated by a focused pump pulse (depicted in red) and a wide-field probe pulse (depicted in blue). The reflection from the probe is used to image the surface on a CCD camera.

The experimental procedure is shown in Fig. 3.1. To prepare the gel sample, we mix 1.5 g of gelatin from porcine gel (G2625-100G Sigma-Aldrich) with 15 ml of mili-Q demineralized water at a temperature of approximately 50 °C, after which we pour 3 ml of the hot gel mixture into a plastic container with a 2 cm diameter. We allow the gel to partially set, waiting for 5 minutes at room temperature, after which we gently place a polished fused silica glass substrate ($\lambda/20$) onto the gel surface, as illustrated in Fig. 3.1a. After the gel has fully set, we remove the glass substrate, leaving a small and flat surface (1 cm^2) suitable for ablation experiments. The optical experiments are carried out in the transient reflectivity microscope, previously described in [21] and also in Section 1.2, and summarized in Fig. 3.1b. Single femtosecond laser pulses from an amplified Ti:Sapphire laser are focused on the gel surface using

a microscope objective. The laser pulse duration is 150 fs (full width half-maximum) and the central laser wavelength 800 nm. The objective and the gel are enclosed in a container that allows us to control the atmosphere above the gel. Part of the light from the laser is split off and frequency doubled. These much weaker pulses are delayed using an optical delay line and then also sent through the objective. The reflection from this probe light is imaged using a camera as a function of pump-probe delay.

3.3 Time evolution of gel ablation

Typical results of the transient reflectivity measurements are shown in Fig. 3.2, which were carried out above a gel surface. We interpret the dark disk in the center of this images as the ablation plume that propels upwards, towards the objective. The ring-shaped feature that can be seen concentrically around the disk appears to be associated with a shock-wave in the surrounding atmosphere, as the radius and the strength of the features at a given pulse energy and pump-probe delay can be strongly influenced by changing the composition of the background gas. For the measurements shown here, the background gas was tetrafluorethane (TFE), which produces a particularly strong ring. When air is used as a background gas, the ring is much weaker and when Helium is used, no ring can be observed for the pulse energies used here, as discussed in Section 1.2. An exact study of the behavior of the ring is, however, outside of the scope of this work.

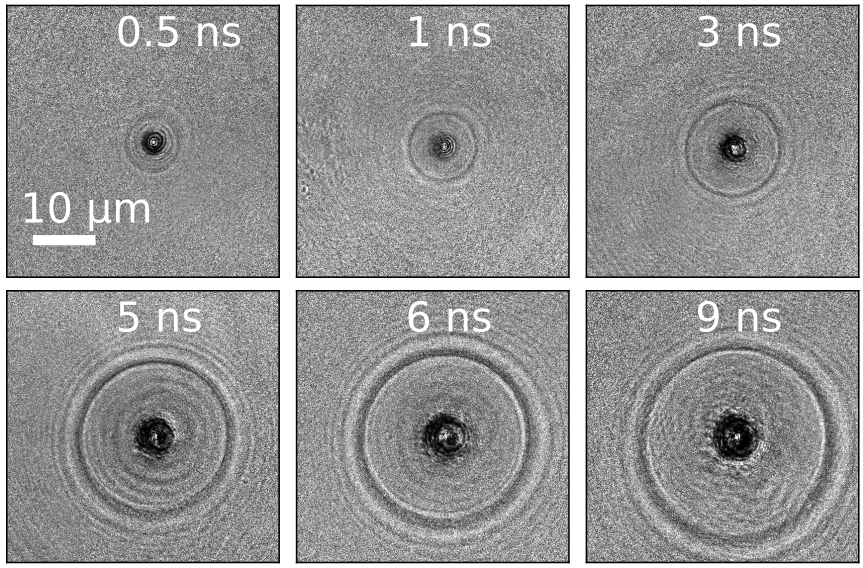

Figure 3.2: Transient reflectivity images obtained at several pump-probe delays, during the ablation of gel in an atmosphere of tetrafluorethane. We clearly note a dark disk in the center, with a ring shaped feature centered around it. The laser energy per pulse was set to be 5 μJ.

3.4 Gel vs Water ablation: Ablation aftermath

Water and gel are to some extent expected to behave similarly under ablation condition; they have comparable mass densities of 1.00 g/cm^3 and 1.10 g/cm^3, respectively. Furthermore, the gel has a refractive index of 1.36-1.38 [34, 35], which is close to that of water. Also, linear optical absorption of both water and gel is negligible at the pump wavelength. However, the nonlinear optical properties of the gel are largely unknown. To compare water and gel, we therefore determine the radius of the black disk and the ring by performing an azimuthal average of each image, measured at a fixed pump-probe delay of 10 ns and as a function of the incident pulse energy. The result of this analysis is shown in Fig. 3.3. The blue symbols in the graph correspond to the radius of the black disk and the orange symbols to the radius of the ring. The differences in properties of water and gel apparently have only a minor influence on the expansion of the ablation plume, as we clearly see that there is no significant difference between the behavior of those features when measured on gel (closed symbols) or water (open symbols). This strongly suggests that the ablation behavior of gel and water are also very similar in this energy range. Crucially this means that we can combine what we can learn from gel with what we already know about water, as we will do in the following. In particular, this means that we can estimate the amount of material that is ablated (in either water or gel) by measuring the surface topography of the gel after ablation. We measure this topography using the optical profilometer. Typical result of such measurements are shown in Fig. 3.4. The top row shows topography maps of two ablation craters created by a single laser pulse with energies of 5.0 μJ (Fig. 3.4(a)) and 2.5 μJ (Fig. 3.4(b)). Note that these maps contain some roughness around the crater (caused by the initial surface roughness), which limit the accuracy of the measurements discussed below. The bottom row shows the associated azimuthal averages. From these averages, we can obtain the depth of the crater (measured from the bottom of the crater to the top of the rim), the radius (which we define as the width measured halfway between the bottom of the crater to the top of the rim) and the crater volume (which we define as the volume inside the radius).

The results of this analysis are shown in Fig. 3.5. The top graph shows the depth (blue points, left y-axis) and the radius (orange points, right y-axis) as a function of the incident pulse energy. The error bars are the standard deviation taken over up to three craters created using the same pulse energy.

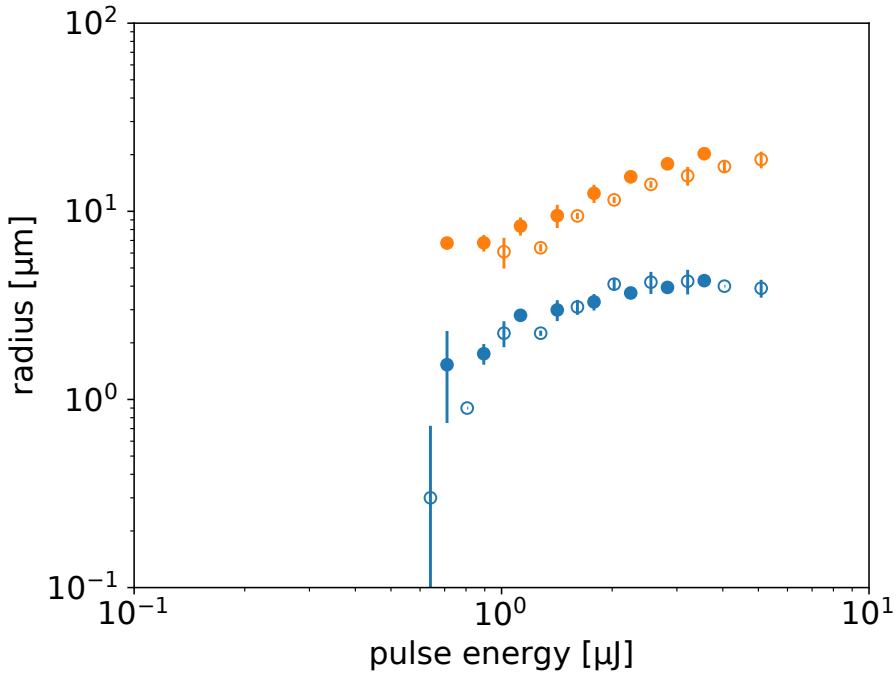

Figure 3.3: This graph compares the radii of modification of water (open symbols) and gel (closed symbols), measured at a pump-probe delay of 10 ns. The blue symbols correspond to the radius of the dark disk, the orange symbols correspond to the radius of the ring shaped feature.

The bottom graph shows the estimate of the removed volume (blue points, left y-axis). The volume seems to show a subtle threshold behavior around an incident pulse energy of 2.5 μJ, although we should be careful not to attach to much value to that single data point.

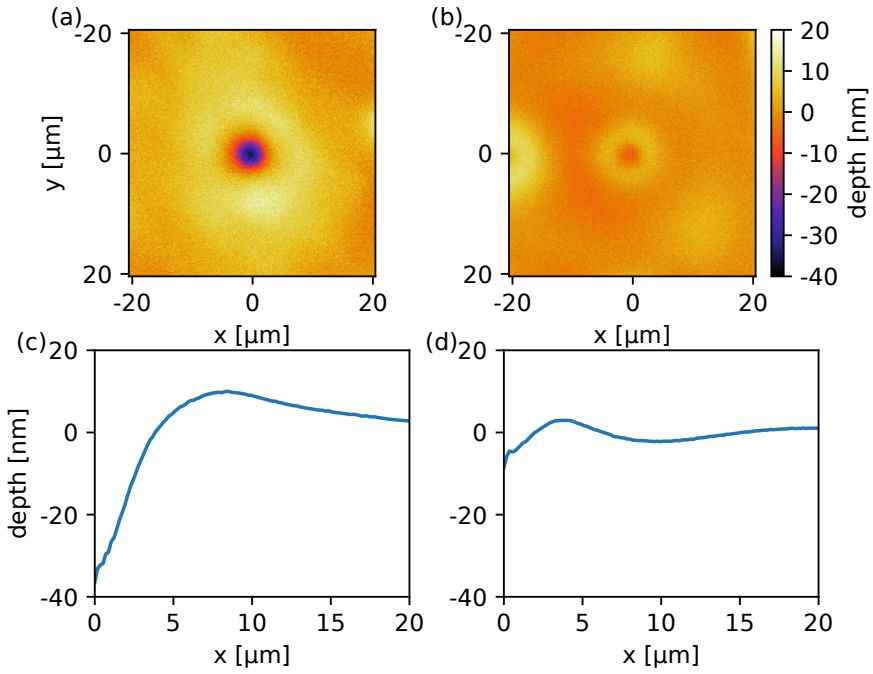

Figure 3.4: Surface topography of the gel after strong (a) and gentle (b) ablation, obtained using optical profilometry. The bottom panels (c) and (d) show corresponding azimuthal averages around the center of the ablation craters.

As we have argued above, the behaviour of gel and water appear sufficiently similar to combine what we can learn from experiments on the ablation of gel with what we already understand about the ablation of water. We therefore use our previously established finite-difference-time-domain model for the ablation of water [27], briefly described in Section 1.3, to compute energy that is absorbed by the water for each of the experimentally used incident pulse energies. Specifically, we compute the part of the energy that is stored in the form of the heat of the resulting electron plasma. These energies are indicated as the ticks on the top x-axis and also shown in the bottom graph (orange

circles, right y-axis). Note that the scale of the right y-axis is chosen such that the electron heat for that pulse energy coincides with the average measured crater volume.

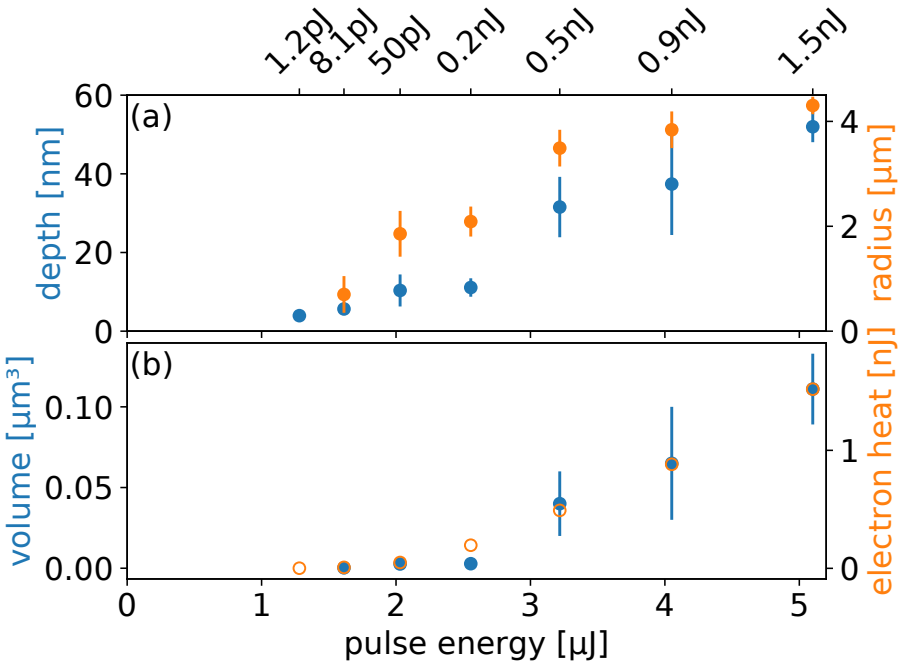

Figure 3.5: (a) Crater depth (blue symbols, left axis) and radius (orange symbols, right axis) as a function of incident pulse energy. (b) Crater volume (solid blue symbols, left axis) and the electron heat as obtained from model calculations (open orange symbols, right axis) as a function of incident pulse energy.

Remarkably, the measured volume and the computed electron heat coincide over a large range of incident pulse energies. In fact, the overlap is fortuitously good, given the error bars. This suggests that under the conditions of our experiment, the ablation plume has a specific energy that is independent of incident pulse energy. If we subtract from this specific energy the latent heat of evaporation and assume the remainder is used as kinetic energy of the plume, we find a velocity for the plume of 5 ± 1km/s for the three energies above the apparent threshold at 2.5 μJ. As this number is highly supersonic, it is likely that most of the energy is indeed converted into vertical kinetic energy. As

a result of that and the strong focusing we employ in our setup, the plume in our experiment is expected to develop into a highly elongated shape, in contrast to the well studied case of weak focusing [15, 16, 19, 20].

It is as of yet unclear to us why the effective velocity we find would be independent of, or at least insensitive to, the incident pulse energy. Furthermore, we currently do not know what determines this velocity. One could argue that it should be related to the sound velocity in the super-critical and highly ionized material in the ablation zone. Yet this sound velocity is hard to obtain independently.

3.5 Conclusion

In conclusion, we have shown that the ablation plume dynamics of water and aqueous gel are extremely similar. We have used this similarity to combine aftermath results of the ablation of gel with numerical models established to describe the absorption of ultra-short laser pulse by water. This has allowed us to estimate the initial velocity of the ablation plume, which is surprisingly insensitive to the absorbed laser energy. This surprising feature could in future be studied further using more intricately shaped ablation beams, possibly combined with side-imaging or other methods.

Bibliography

[1] R. R. Gattass and E. Mazur, "Femtosecond laser micromachining in transparent materials," Nat. Photonics **2**, 219–225 (2008).

[2] P. Balling and J. Schou, "Femtosecond-laser ablation dynamics of dielectrics: basics and applications for thin films," Rep. Prog. Phys. **76**, 036502 (2013).

[3] L. Englert, B. Rethfeld, L. Haag, M. Wollenhaupt, C. Sarpe-Tudoran, and T. Baumert, "Control of ionization processes in high band gap materials via tailored femtosecond pulses," Opt. Express **15**, 17855–17862 (2007).

[4] J. Hernandez-Rueda, J. Clarijs, D. van Oosten, and D. M. Krol, "The influence of femtosecond laser wavelength on waveguide fabrication inside fused silica," Appl. Phys. Lett. **110**, 161109 (2017).

[5] M. F. Yanik, H. Cinar, H. N. Cinar, A. D. Chisholm, Y. Jin, and A. Ben-Yakar, "Functional regeneration after laser axotomy," Nature **432**, 822 (2004).

[6] A. Vogel, J. Noack, G. Hüttman, and G. Paltauf, "Mechanisms of femtosecond laser nanosurgery of cells and tissues," Appl. Phys. B **81**, 1015–1047 (2005).

[7] M. H. Niemz, *Laser-Tissue Interactions* (Springer, 2007), 4th ed.

[8] H. A. Collins, M. Khurana, E. H. Moriyama, A. Mariampillai, E. Dahlstedt, M. Balaz, M. K. Kuimova, M. Drobizhev, V. X. D. Yang, D. Phillips, A. Rebane, B. C. Wilson, and H. L. Anderson, "Blood-vessel closure using photosensitizers engineered for two-photon excitation," Nat. Photonics **2**, 420–424 (2008).

[9] S. X. Guo, F. Bourgeois, T. Chokshi, N. J. Durr, M. A. Hilliard, N. Chronis, and A. Ben-Yakar, "Femtosecond laser nanoaxotomy lab-on-a-chip for in vivo nerve regeneration studies," Nat. Methods **5**, 531–533 (2008).

[10] Z. Nagy, A. Takacs, T. Filkorn, and M. Sarayba, "Initial Clinical Evaluation of an Intraocular Femtosecond Laser in Cataract Surgery," J. Refract. Surg. **25**, 1053–1060 (2009).

[11] R. R. Krueger, J. S. Krasinski, C. Radzewicz, K. G. Stonecipher, and J. J. Rowsey, "Photography of shock waves during excimer laser ablation of the cornea. Effect of helium gas on propagation velocity," Cornea **12**, 330–334 (1993).

[12] G. Paltauf and H. Schmidt-Kloiber, "Photoacoustic cavitation in spherical and cylindrical absorbers," Appl. Phys. A **68**, 525–531 (1999).

[13] C. P. Cain, C. A. Toth, G. D. Noojin, D. J. Stolarski, R. J. Thomas, and B. A. Rockwell, "Thresholds for retinal injury from multiple near-infrared ultrashort laser pulses," Health physics **82**, 855–862 (2002).

[14] A. L. Klein, W. Bouwhuis, C. W. Visser, H. Lhuissier, C. Sun, J. H. Snoeijer, E. Villermaux, D. Lohse, and H. Gelderblom, "Drop Shaping by Laser-Pulse Impact," Phys. Rev. Applied **3**, 44018 (2015).

[15] X. Zeng, X. Mao, S. S. Mao, S.-B. Wen, R. Greif, and R. E. Russo, "Laser-induced shockwave propagation from ablation in a cavity," Appl. Phys. Lett. **88**, 61502 (2006).

[16] A. Vogel, S. Busch, and U. Parlitz, "Shock wave emission and cavitation bubble generation by picosecond and nanosecond optical breakdown in water," J. Acoust. Soc. Am. **100**, 148–165 (1996).

[17] T. Juhasz, X. H. Hu, L. Turi, and Z. Bor, "Dynamics of shock waves and cavitation bubbles generated by picosecond laser pulses in corneal tissue and water," Lasers Surg. Medicine **15**, 91–98 (1994).

[18] C. B. Schaffer, N. Nishimura, E. N. Glezer, A. M.-T. Kim, and E. Mazur, "Dynamics of femtosecond laser-induced breakdown in water from femtoseconds to microseconds," Opt. Express **10**, 196–203 (2002).

[19] C. Sarpe-Tudoran, A. Assion, M. Wollenhaupt, M. Winter, and T. Baumert, "Plasma dynamics of water breakdown at a water surface induced by femtosecond laser pulses," Appl. Phys. Lett. **88**, 261109 (2006).

[20] B. D. Strycker, M. M. Springer, A. J. Traverso, A. A. Kolomenskii, G. W. Kattawar, and A. V. Sokolov, "Femtosecond-laser-induced shockwaves in water generated at an air-water interface," Opt. Express **21**, 23772–23784 (2013).

[21] M. Vreugdenhil, D. van Oosten, and J. Hernandez-Rueda, "Dynamics of femtosecond laser-induced shockwaves at a water/air interface using multiple excitation beams," Opt. Lett. **43**, 4899–4902 (2018).

[22] J. Hernandez-Rueda and D. van Oosten, "Dynamics of Ultrafast Laser Ablation of Water," arXiv preprint arXiv:1810.06946 (2018).

[23] A. Vogel, "Nonlinear absorption: intraocular microsurgery and laser lithotripsy," Phys. Med. Biol. **42**, 895–912 (1997).

[24] C. Sarpe, J. Köhler, T. Winkler, M. Wollenhaupt, and T. Baumert, "Real-time observation of transient electron density in water irradiated with tailored femtosecond laser pulses," New J. Phys. **14**, 075021 (2012).

[25] N. Linz, S. Freidank, X.-X. Liang, H. Vogelmann, T. Trickl, and A. Vogel, "Wavelength dependence of nanosecond infrared laser-induced breakdown in water: Evidence for multiphoton initiation via an intermediate state," Phys. Rev. B **91**, 134114 (2015).

[26] T. Winkler, C. Sarpe, N. Jelzow, L. L. H., N. Götte, B. Zielinski, P. Balling, A. Senftleben, and T. Baumert, "Probing spatial properties of electronic excitation in water after interaction with temporally shaped femtosecond laser pulses: Experiments and simulations," Appl. Surf. Sci. **374**, 235–242 (2016).

[27] J. Hernandez-Rueda and D. van Oosten, "Transient scattering effects and electron plasma dynamics during ultrafast laser ablation of water," Opt. Lett. **44**, 1856–1859 (2019).

[28] L. V. Keldysh, "Ionization in the field of a strong electromagnetic wave," Sov. Phys. JETP **20**, 1307–1314 (1965).

[29] B. Rethfeld, "Unified Model for the Free-Electron Avalanche in Laser-Irradiated Dielectrics," Phys. Rev. Lett. **92**, 187401 (2004).

[30] V. E. Gruzdev, "Photoionization rate in wide band-gap crystals," Phys. Rev. B **75**, 205106 (2007).

[31] B. Rethfeld, "Free-electron generation in laser-irradiated dielectrics," Phys. Rev. B **73**, 035101 (2006).

[32] B. Christensen and P. Balling, "Modeling ultrashort-pulse laser ablation of dielectric materials," Phys. Rev. B **79**, 155424 (2009).

[33] J. Hernandez-Rueda, D. Puerto, J. Siegel, M. Galvan-Sosa, and J. Solis, "Plasma dynamics and structural modifications induced by femtosecond laser pulses in quartz," Appl. Surf. Sci. **258**, 9389–9393 (2012).

[34] A. J. Durkin, S. Jaikumar, and R. Richards-Kortum, "Optically Dilute, Absorbing, and Turbid Phantoms for Fluorescence Spectroscopy of Homogeneous and Inhomogeneous Samples," Appl. Spectrosc. **47**, 2114–2121 (1993).

[35] H. G. Akarçay, S. Preisser, M. Frenz, and J. Rička, "Determining the optical properties of a gelatin-TiO_2 phantom at 780 nm," Biomed. Opt. Express **3**, 418–434 (2012).

4 Shaped light beams for laser processing of materials

Abstract. In semiconductor industry, laser ablation has great potential for application throughout the fabrication process. However, uncontrolled debris produced during the process leads to a great reduction in the wafer quality and therefore impedes widespread adoption of the technology. We propose that spatial beam shaping can lead to new ways to control the ablation process and thereby the ejection of debris. As a first step, we demonstrate high-fidelity spatially shaped beam patterns through a high numerical aperture objective.

4.1 Motivation

Laser processing of materials is heavily utilized in science as well as in industry [1], ranging from macro scale manufacturing [2] to micro/nano fabrication [3]. A special use case is in the semiconductor industry. As this industry is pushing for ever smaller structures to pursue Moore's law [4], one step taken on this road is the use of laser ablation to dice silicon wafers instead of "big" metal blades [5, 6]. The advantages of using a laser over mechanical blades are plenty: high precision, small cut size, less damage and high cutting speed. Most importantly, multiple cuts can be made at the same time using laser ablation, something that is impractical with conventional cutting techniques. All these advantages lead to higher throughput. However, there are the issues of uncontrolled debris produced during ablation [5] and of potential structural brittleness of the devices after dicing [6]. To control this process, we have to understand the physics underlying the ablation process. We propose that spatial beam shaping will be a tool to control the ablation of the wafers.

During femtosecond laser ablation, the spatial distribution of light onto the surface of the sample can have a profound impact on the shape of the crater. Simply put, the parts of the sample that are exposed to the high intensity center of the laser beam might be heated to such an extent that they vapor-

ize, whereas the surface exposed to the tails of the beam profile might only be molten under the influence of the laser. Furthermore, parts deeper into the sample will generally remain cooler than parts close to the surface, resulting in a molten layer of material in between the solid material and the vaporized material, as illustrated in Fig 4.1(a). Obviously, the rapid expansion of the vapor (discussed in Chapters 2 and 3) will result in a recoil pressure that can expel the liquid. As illustrated in Fig 4.1(b), a TopHat like intensity distribution would minimize the size of the liquid pool surrounding the vapor. This can potentially be used to suppress debris formed by the expulsion of liquid material. Besides this practical application, shaped beams can also be used to better understand the mechanisms that cause liquid flow during ablation. As mentioned before, one such mechanism is the recoil pressure. Another mechanism is so-called Marangoni flow [7], which is caused by temperature gradients in the liquid. Being able to apply precise gradients on top of the TopHat intensity distribution, which we call a TiltedHat pattern, can assist in inducing and studying Marangoni flow.

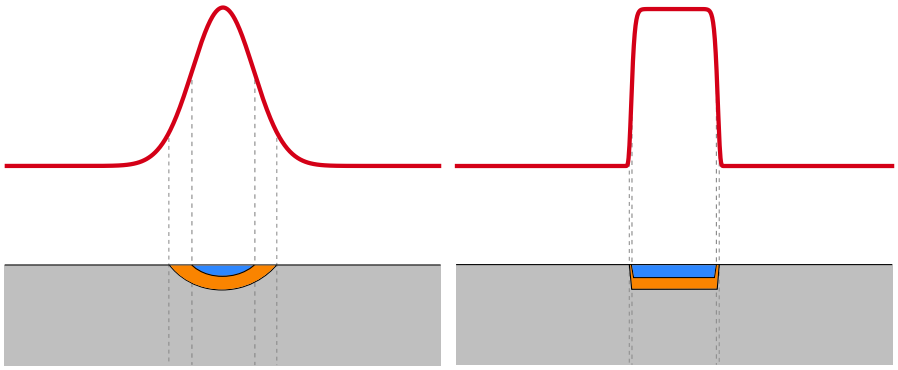

Figure 4.1: Ablation of semiconductors. The left figure is with a Gaussian intensity distribution. The right figure is with a TopHat intensity distribution. Ablation plumes and molten materials are depicted in blue and orange colors respectively.

In this chapter, we develop a beam shaping method for the ablation applications using high numerical aperture (NA) optics. We propose to use a liquid crystal spatial light modulator (LCoS SLM or SLM in short) in combination with digital holography to perform beam shaping. Such a SLM is an

ideal candidate due to the ease of implementation and high versatility. Most importantly it has a high light efficiency compared to the efficiencies reached with other adaptive optics elements such as digital mirror devices (DMDs). To program the SLM, we use the high-fidelity Mixed-Region-Amplitude-Freedom (MRAF) algorithm [8] to create the intensity pattern. It is an ideal choice for ablation due to the fact that it can create intensity profiles with high-fidelity and a sharp boundary between ablation region and outside region, where there are only low intensity speckle below the ablation threshold. High-fidelity and the sharp boundary are absolutely necessary criteria for ablation. First, we test our modified MRAF algorithm both numerically and experimentally at the Fourier plane of a 4-f system. We then demonstrate our beam shaping method by achieving high-fidelity TopHat patterns through a high NA objective as a first step towards the ablation applications.

4.2 Beam shaping

Over the last two decades, beam shaping in laser processing of materials has developed into a mature field that is highly relevant to industry [9]. Many methods to shape the light beam have been developed so far [10]. Laser processing/ablation of material surfaces using static optical elements such as refractive optical elements (ROEs) [11–13] and diffractive optical elements (DOEs) [14–16] have been demonstrated. With the advent of adaptive optical elements such as DMDs and SLMs, it is now possible to dynamically control the spatial, temporal and polarization attributes of the laser beam [9]. Ablation with a deformable mirror [17] has been demonstrated, but the degree of freedom of the mirror to shape the light field is very limited compared to the other adaptive optics elements such as DMDs and SLMs. Therefore it is hard to create complicated structures. A DMD is a possible candidate to spatially shape the beam. TopHat patterns with a high-fidelity [18] have been demonstrated; however, a low experimental light efficiency (below 10 percent) [18,19] prohibits its usage in ablation experiments. Ablation with SLMs has been demonstrated [20–25]. Especially TopHat multi-shot ablation has been demonstrated [24, 25]. The studies used the normal Gerchberg-Saxton (GS) algorithm which suffers notoriously from speckle [24], thus the authors had to use an averaging method to suppress the effects of speckle in the ablation pattern. Such an averaging method is obviously unsuitable for single-shot ablation studies. Therefore, we show the MRAF algorithm is the best possible

choice currently available in terms of light efficiency and creating high-fidelity targets for single-shot ablation studies.

4.2.1 MRAF TopHat/TiltedHat algorithm

In holographic beam shaping [26], the incident light intensity distribution at the SLM plane is often known to be a Gaussian laser spot. We also know the desired intensity pattern in the Target plane, for instance a TopHat or TiltedHat pattern. The challenge is to determine a phase distribution on the SLM, known as a kinoform, such that the light field with that phase pattern goes through all optical elements creating the desired intensity at the Target plane, which is usually chosen to be the Fourier plane of the SLM [26]. There is no constraint on the phase at either planes. The iterative Fourier transform algorithm (IFTA) solves the problem by using this phase freedom to minimize the difference between the desired intensity pattern and the calculated intensity distribution at each iteration. A well-known example is the GS algorithm. The method that is currently considered to be superior, is the MRAF algorithm, which is a modified GS algorithm first proposed to create arbitarily shaped holographic atomic traps [8, 27, 28]. Other possible solutions exist; however, each has disadvantages: the genetic algorithm which is computationally demanding [29] and the direct search method, which uses only a few phase levels and is therefore not good for creating complicated structures [30, 31]. New methods have been introduced such as the conjugate gradient method [32], but its TopHat light efficiency appears too low to make it practical. Machine learning combined with the IFTA is proposed [33] but it has only been applied for creating simple intensity control of an array of points.

In this work, we use a modified version of the MRAF algorithm. In the MRAF algorithm, the Target plane is divided into two sections [27]: the noise region, where the light amplitude is uncontrolled, and the canvas, where the desired amplitude (TopHat/TiltedHat) is imposed at each iteration, as depicted in Fig. 4.2. The original MRAF paper [8] introduces an ad-hoc parameter to control the relative amplitude in the canvas and noise region, from which the authors later compute the efficiency, i.e. the power in the target pattern divided by the total incident power. We rewrite the constraint such that we rather use the efficiency as a parameter directly, which we call η_{Target}.

Figure 4.3 shows a typical computational result of a TopHat pattern created with MRAF. We constrain the amplitude of the target pattern such that it

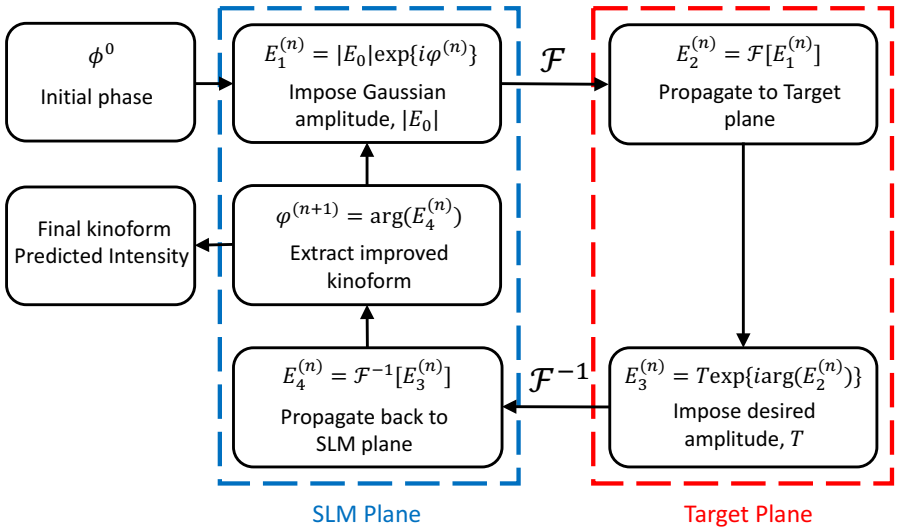

Figure 4.2: Diagrammatic representation of the MRAF algorithm. F represents the Fourier transform [8, 26, 27].

contains 40 percent of the total incident power, i.e. η_{Target}=0.4. Figure 4.3(a) and (b) show the TopHat pattern imposed at the Fourier plane during the first iteration and a calculated high-fidelity TopHat after 1500 iterations, respectively. Figure 4.3(c) and (d) show the horizontal and vertical cross sections inside the canvas region of Fig. 4.3(a) and (b) plotted together. We also take into account that during an experiment there will always be zeroth diffraction order or unshaped light reflected from the SLM, by shifting the pattern away from the center of the Fourier plane with an appropriate choice of the initial phase [8]. Due to this shift, MRAF cross sections show more noise on the left edge. A TiltedHat pattern computed using similar parameters is shown in Fig. 4.4. Unlike the GS algorithm, which is known to create speckles in the patterns already in the calculation [24], the MRAF algorithm produces the high-fidelity TopHat/Tilted patterns without any speckle.

Figure 4.5 presents numerical tests we have done with MRAF. Figure 4.5(a) shows the RMS error of the TopHat and TiltedHat as a function of the efficiency parameter η_{Target}. Both TopHat and TiltedHat results have very low RMS error (below 10 percent) for very high efficiency parameters. The high fidelity of the algorithm, even with a high light efficiency η_{Target}, is obviously

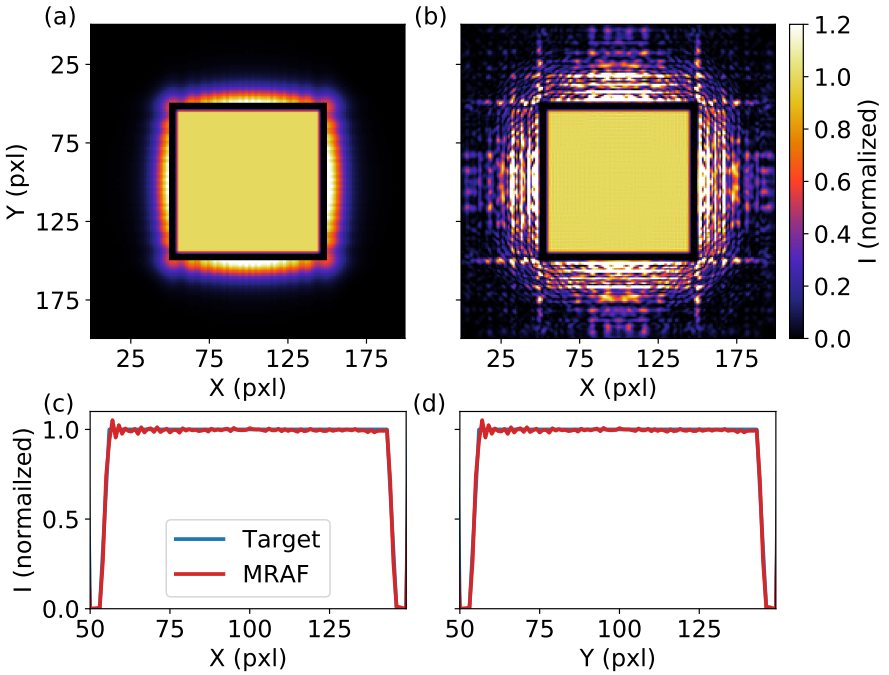

Figure 4.3: A TopHat pattern computed with MRAF. (a) TopHat pattern (normalized) with 40 percent efficiency (η_{Target}=0.4) is imposed in the Fourier plane during the first iteration. (b) Final calculated TopHat pattern (normalized by the maximum intensity of TopHat pattern) in the Fourier plane after 1500 iterations. (c) is horizontal and (d) is vertical cross sections, respectively, inside the canvas region from (a) and (b) plotted together.

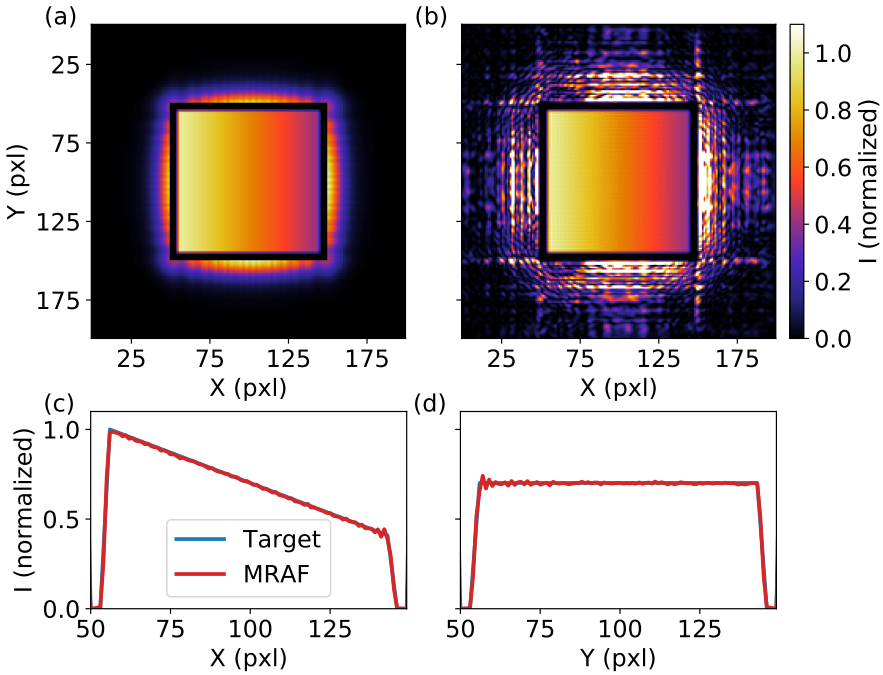

Figure 4.4: A TiltedHat pattern computed with MRAF. (a) TiltedHat pattern (normalized) with 40 percent efficiency (η_{Target}=0.4) is imposed in the Fourier plane during the first iteration. (b) Final calculated TiltedHat pattern (normalized by the maximum intensity of TiltedHat pattern) in the Fourier plane after 1500 iterations. (c) is horizontal and (d) is vertical cross sections, respectively, inside the canvas region from (a) and (b) plotted together.

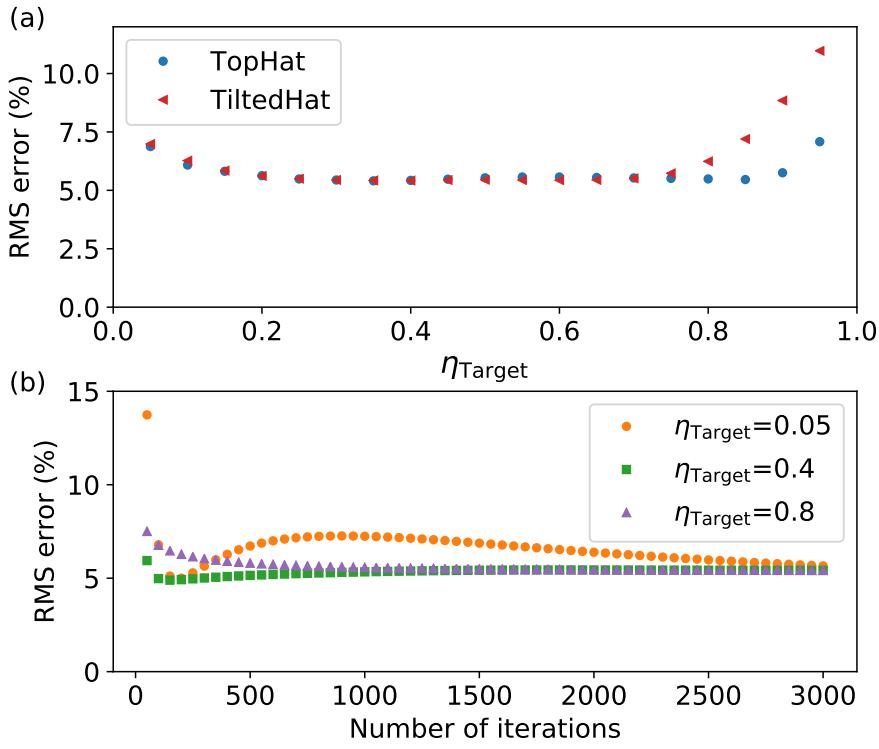

Figure 4.5: Characterization of the MRAF algorithm. (a) RMS error of the TopHat and TiltedHat patterns are shown for different values of the efficiency parameter η_{Target}. (b) RMS error for the TopHat pattern with three different efficiency parameter values, calculated as a function of a number of iterations.

crucial for ablation experiments. For ablation to occur, the intensity (or fluence) of the pattern must be higher than the ablation threshold. In other words, the higher the light efficiency of the pattern, the better for ablation experiments. Also the fidelity of the pattern (RMS error) is important to control the depth of the crater created by ablation, as the intensity inside the pattern determines the depth.

The plot shows that until an efficiency parameter of 0.7, the TopHat and TiltedHat patterns have the same RMS error. Therefore we perform the rest of the tests with only the TopHat pattern. In Fig. 4.5(b), we show the RMS error of the TopHat pattern as a function of a number of iterations we use in the algorithm at three different values for the light efficiency parameter. It appears the higher the light efficiency parameter, the faster the algorithm converges even though the IFTA does not formally guarantee convergence [32]. Even at a small value of the light efficiency parameter, η_{Target}=0.05, the algorithm converges eventually (after 3000 iterations). Also it validates that 1500 iterations is enough for most of the η_{Target} values we are interested in. We did not test other parameters such as the size of the zero padding surrounding the SLM plane, because extensive tests have already been done [8, 27]. From these simulations, we see that the MRAF algorithm can create the high efficiency (0.7) patterns with low RMS error (5%) within reasonable calculation times.

4.2.2 Experimental setup

The setup used in the beam-shaping experiments is shown in Fig. 4.6. Light from a continuous wave fiber coupled diode laser[1] with a wavelength of 785 nm is split into two beams with a polarizing beam splitter. One is blocked with a beam-dump. The other is used to illuminate a phase-only SLM[2]. The SLM is imaged onto the back focal plane of an objective[3] with a 4-f system. The SLM is used to imprint a phase pattern on the beam. The inset of Fig. 4.6 shows a typical phase pattern used in the experiments. The shaped beam passes through the objective, thus leading to a strongly focused intensity pattern at the Target plane. The light reflected from the Target plane is captured by the objective and imaged on an electron multiplying CCD camera[4] using a f=300

[1] Thorlabs, LP785-SF100
[2] Holoeye Pluto-BB for 700-1000nm
[3] Nikon CFI60, 100x, NA=0.8
[4] Andor, Ixon 885

mm tube lens.

The configuration of the setup is similar to the one shown in Fig. 2.1. The main difference is that we use an additional CCD camera[5] to image the intermediate image plane. The advantage of using the 4-f system is that it offers an image plane where we can physically block the zeroth diffraction order or unshaped light, as well as high intensity light from the noise region that is detrimental to the ablation experiments. The auxiliary camera provides an extra capability of monitoring the light pattern going through the objective as temporal instability of the SLM could cause intensity fluctuations in the pattern.

4.2.3 SLM calibration

A correct SLM response is crucial for generating a high-fidelity intensity pattern at the Target plane, as the phase patterns we use are highly complex, as shown in the inset of Fig. 4.6. The SLM has liquid crystals sandwiched between two planes that are connected to electrodes to which DC voltages are applied [26]. The backplane is reflective while the front plane is transmissive. The applied voltages change the orientation of the liquid crystals, thereby changing the effective refractive index of the liquid crystals. To set the applied voltage, each SLM pixel is controlled digitally by a gray value, an 8-bit value that addresses the SLM pixels which is converted into voltage by the SLM driving hardware [34].

The phase modulation of the SLM is given by [26, 35]

$$\phi = \frac{4\pi}{\lambda} d\Delta n, \tag{4.1}$$

where λ is the wavelength used, d is the thickness of the liquid crystal layer, and $\Delta n = n_{\text{eff}} - n_{\text{o}}$ is the difference between the effective and ordinary refractive index of the liquid crystals. From this equation, one can see that the phase response of the SLM depends on the wavelength of the light and therefore has to be calibrated for a given λ. Two main calibration methods have been published, an interferometry based method [36] and diffraction based method [35]. We use a simple diffraction based method. A binary grating with a certain gray level is displayed on the SLM. The intermediate image plane is recorded with the auxiliary CCD camera. We choose the period of the grating such that $\pm 1^{\text{st}}$ diffraction orders are as far away from each other

[5] Basler, Dart daA1600-60um

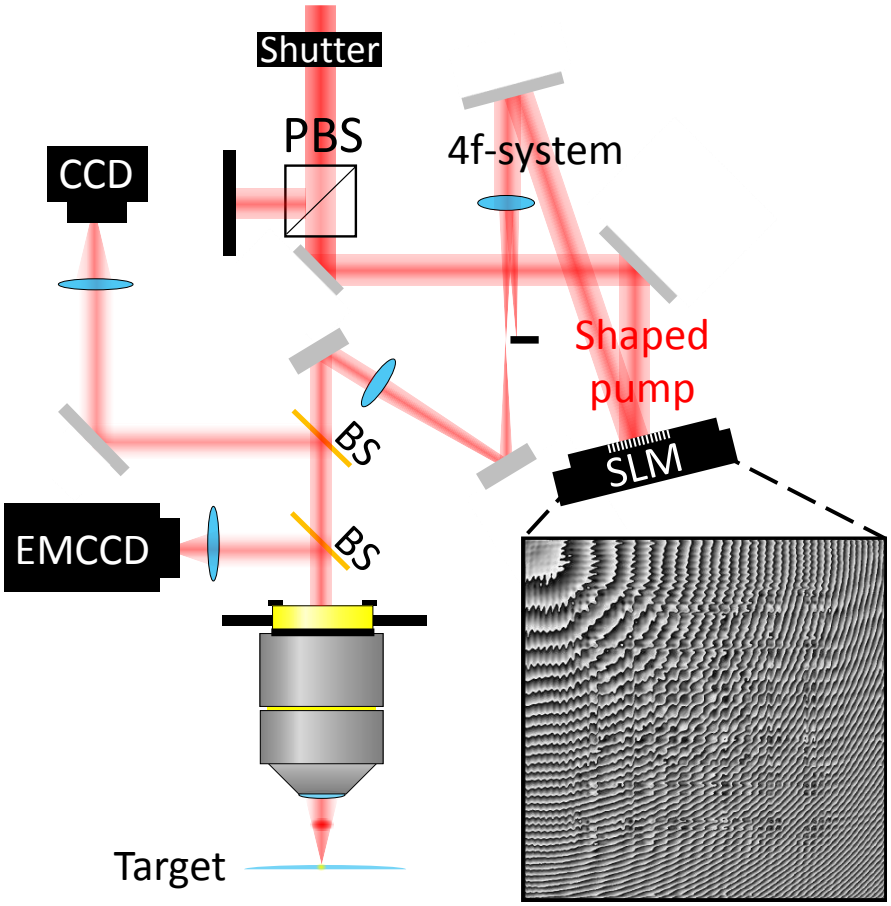

Figure 4.6: Schematics of the experimental setup. Light from a CW laser is reflected on a spatial light modulator (SLM) and acquires an additional phase. The intermediate image plane, where the zeroth order light is blocked with a physical aperture, is imaged onto a CCD camera. The SLM plane is imaged onto the back focal plane of a microscope objective, leading to the desired pattern at the Target plane. The image in the Target plane is recorded in reflection with an EMCCD camera. The inset shows the final calculated kinoform (1000 by 1000 pixels) corresponding to the calculation shown in Fig. 4.3. The phase profile is shown in grayscale where white and black represent 2π and 0 phase, respectively.

as possible, similar to the top row of Fig. 2.2. We change the gray value from 0 to 255 and integrate the 1st order intensity. The resulting signal in the $\pm 1^{st}$ diffraction orders should ideally be proportional to $\sin^2(\phi/2)$, where ϕ is the modulated phase or gray value [35]. Therefore, we look for the back and front plane voltage values of the SLM such that the 1st order intensity covers the phase values from 0 to 2π as much as possible. At the same time, it should fit with the sine squared function as well. In Fig. 4.7(a), we plot the first order intensity as a function of the gray value for the optimum voltage values. Our measurement data fit well with the sine squared function. Figure 4.7(b) shows corresponding phase response as a function of the gray value. After the calibration, the phase response is accurate within 0.08 rad.

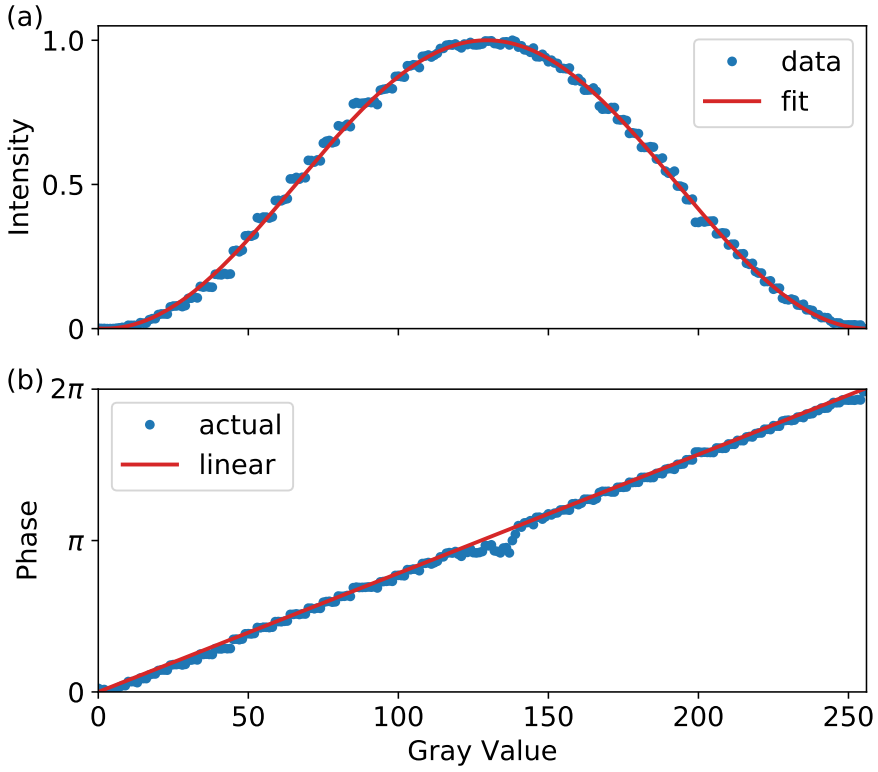

Figure 4.7: SLM calibration. (a) The first order intensity (normalized) as a function of the gray levels of SLM response. The continuous line is a fit for a sine squared function. (b) Dots represent the actual phase response of the SLM while the line is an ideal linear response.

4.2.4 TopHat with CW laser

We demonstrate the creation of a TopHat pattern using the CW laser imaged at the intermediate image plane. Figure 4.8(a) shows the experimental TopHat pattern corresponding to the computed case shown in Fig. 4.3(b). The vertical and horizontal cross sections of the pattern are also shown. The dashed lines, where the cross sections are taken, are superimposed on the pattern using corresponding colors. From the figure, one can see that we overexposed the zeroth order at the top-left corner of the pattern and the noise region surrounding the pattern. The zeroth order and the noise region can be easily blocked with a physical aperture at the intermediate image plane during ablation experiments (see Fig. 4.6). There is an intensity gradient from the top-left corner to the bottom-right corner due to the fact that the diffraction efficiency of the SLM decreases as a function of the deflection angle with respect to the zeroth order. This is a known effect due to the absence of sharp edges in the phase profile of the physical device. Feedback can be used to fix this type of error, as well as typical aberrations of an optical system [37]. However, even without feedback control, our algorithm creates a high-fidelity pattern. The zero region between the pattern and the noise region has a very low intensity across the cross sections, which is crucial for ablation studies, as all signal in this region must be below the ablation threshold. The size of the region stays the same, showing a clear separation between the signal and noise regions. There is a small deviation from the square shaped pattern due to aberrations in the optics. From the cross sections, we see the TopHat pattern shrinks in the X direction, which we attribute to Petzval field curvature of the relay lenses.

Besides the aberration, the main error in the pattern is a semi-regular fringing. To reduce this error, we implemented a slightly low-pass filtered TopHat pattern in the simulation, mimicking the finite NA of the system. Figure 4.8(b) shows an experimental realization of the pattern and vertical as well as horizontal cross sections. The low pass filtering of the TopHat in the simulation does not have a significant influence on the final experimental result, therefore we do not use the low pass filtering in following experiments. According to Ref. [27], the fringing error can be caused by the fact that the Fraunhofer approximation is used in the MRAF algorithm. The authors of Ref. [27] therefore use a Helmholtz propagator instead of the simple Fourier transform. This is not implemented in our case.

Figure 4.9 presents a systematic study of the experimental realization of the

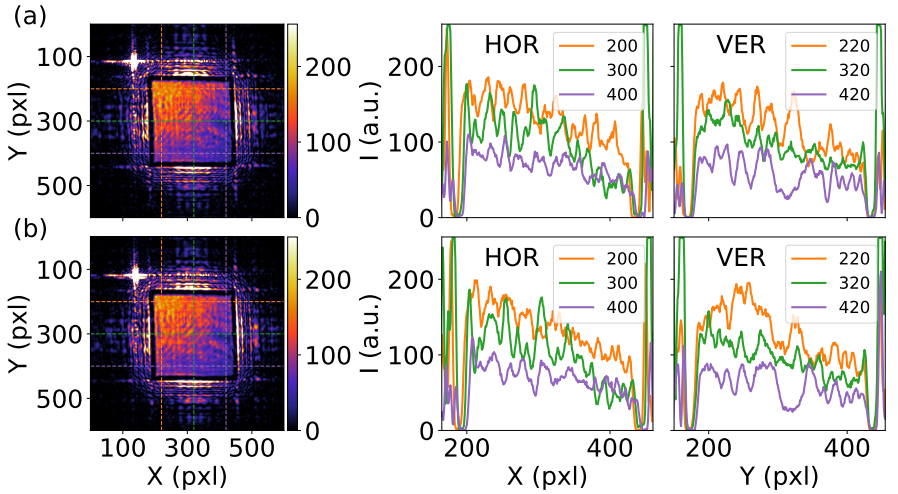

Figure 4.8: Experimental realization of the TopHat pattern. (a) Experimental TopHat intensity pattern (background subtracted) corresponding to Fig. 4.3(b) at the intermediate image plane. The graphs are horizontal (HOR) and vertical (VER) cross sections of the pattern. The positions where the cross sections were taken are indicated on top of the pattern with the dashed lines and same colors. (b) The slightly low-pass filtered TopHat pattern (background subtracted) and corresponding cross sections. Here 1 pixel (pxl) is ∼13 μm.

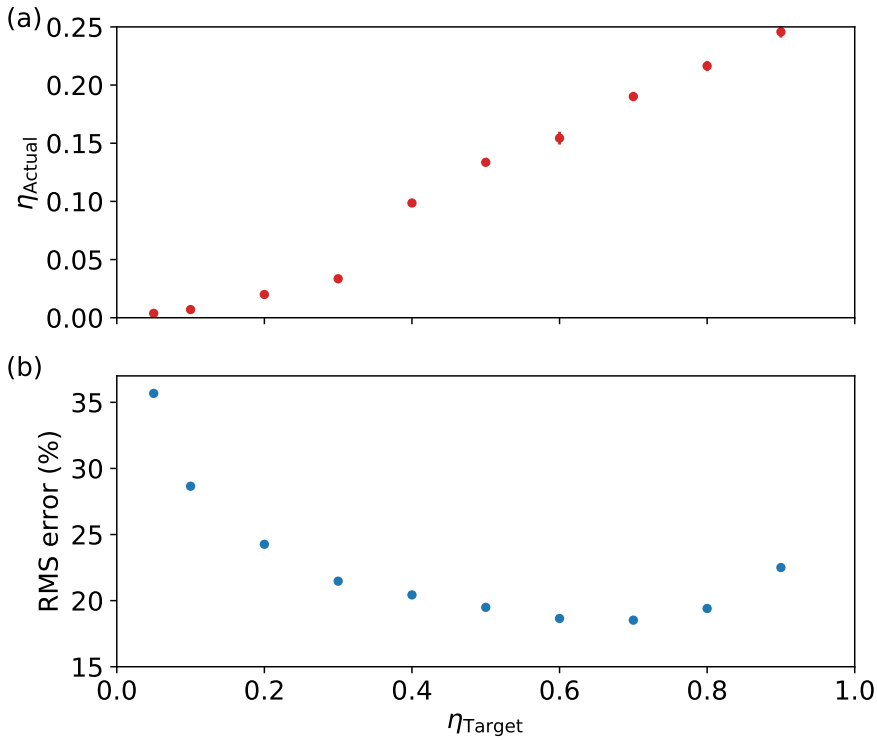

Figure 4.9: (a) The experimental light efficiency and (b) RMS error of the TopHat pattern as a function of the efficiency parameter.

TopHat pattern computed with MRAF. In Fig. 4.9(a), the actual experimental light efficiency of the TopHat pattern is plotted as a function of the light efficiency parameter (η_{Target}). The experimental light efficiency is measured as the ratio of the beam power in front of the SLM and the power going into the TopHat pattern. We note that the experimental efficiency is approximately a factor of 3 lower than the efficiency set in the calculation. This is due to the fact that the SLM has a specular reflection and imperfect diffraction efficiencies [34], and there is a loss in the optics. Figure 4.9(b) shows the corresponding RMS error. In this analysis, we took out the aforementioned intensity gradient in the pattern numerically, which can be achieved in the experiment with the feedback-loop [37], and calculated the RMS error based on the remaining fluctuations. The experimental RMS error closely follows the trend of the predicted RMS error, depicted in Fig. 4.5(a), showing the fidelity of our algorithm. Based on the result, we choose the highest light efficiency pattern with the lowest RMS error for experiments presented in the remainder of this chapter. This corresponds to the TopHat pattern with η_{Target}=0.7.

4.3 Towards fs-laser ablation: Focusing through high NA objective

In this section, we demonstrate the imaging of the TopHat pattern through the high NA objective. The SLM plane is imaged on the back focal plane of the objective through the 4-f system. However, due to the lenses allowed by the space constraints, there is not enough demagnification necessary for the whole light field to go through the back aperture of the objective. This leads to a loss of information resulting in a low-fidelity TopHat pattern. Therefore we use an aperture in the beam path such that all the light that hits the SLM goes through the objective. Because of this, the efficiency is significantly reduced, which can be remedied in a future version of the setup by a comparison of the beam profile using lenses of different focal lengths.

There are two ways to implement this aperture in the experiment. One can put a physical aperture in the beam path or a digital aperture on the SLM. We implement a combination of these two, which is easier to realize in the experiment. First, we introduce a circular aperture on top of the incident Gaussian light field in the MRAF algorithm, and calculate the kinoform, as shown in Fig 4.10(a) and (b), respectively. Note that the phase outside the

aperture is essentially unconstrained by the algorithm. In the experiment we put a circular digital mask with the same size as the aperture on top of the calculated kinoform, as depicted in Fig 4.10(c). The advantage of this procedure is that the phase mask is always perfectly aligned with the kinoform displayed on the SLM. The phase mask in the experiment effectively works as an intensity mask as all light that hits the flat phase area of the mask is reflected into the zeroth diffraction order.

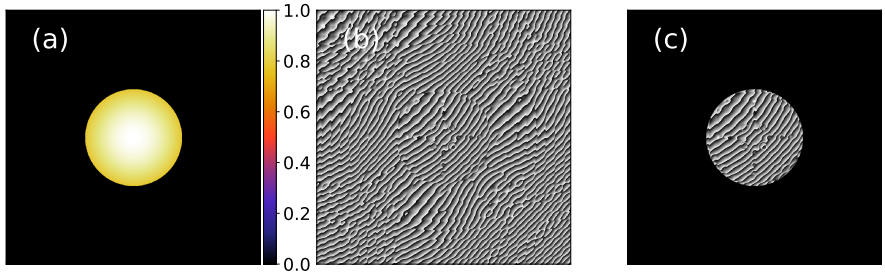

Figure 4.10: (a) Normalized Gaussian intensity apodized by a circular aperture in the MRAF algorithm. (b) Kinoform calculated by the MRAF, shown in grayscale where black and white represent 0 and 2π phase respectively. (c) Apodized kinoform displayed on the SLM in the experiment, shown in grayscale where black and white represent 0 and 2π phase, respectively.

The top row of Fig. 4.11 shows the calculated TopHat patterns with η_{Target}= 0.7 and three different sizes. Due to the small aperture size, the light field in the Fourier plane is constrained to a small region. Thus when we produce a TopHat pattern with a size that exceeds this region, the algorithm leaves dark patches inside the pattern, as shown in the top-left corner of the biggest TopHat pattern. The bottom two rows of Fig. 4.11 show the corresponding patterns recorded at the intermediate image plane and the Target plane, respectively. From the figure, one can see the experimental TopHat patterns closely resemble the predicted intensity patterns in the calculation at both the intermediate image plane and the Target plane. Even the intensity distributions in the noise regions closely resemble the calculation.

The optimal aperture size is obtained based on the experimental pattern at the Target plane. Aperture sizes smaller than the optimum value result in loss of resolution as less degrees of freedom are available in the kinoform. Sizes bigger than the optimum value generate low-fidelity patterns as well. This

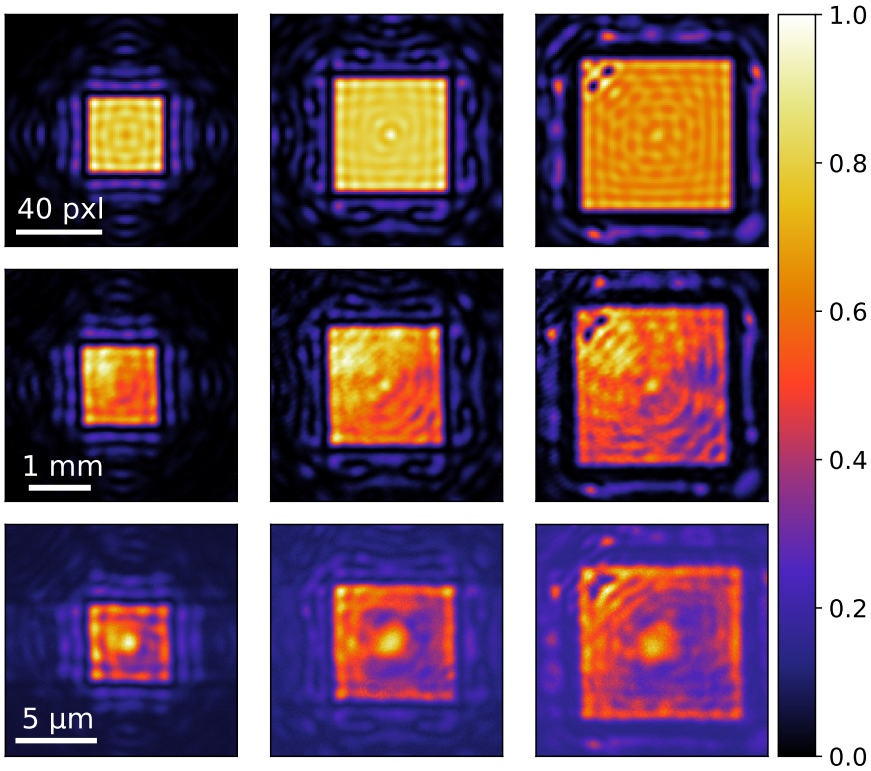

Figure 4.11: TopHat patterns through the objective. Top row shows the calculated TopHat patterns. Middle and bottom rows show the corresponding images recorded at the intermediate image plane and the Target plane, respectively. All images are displayed in normalized intensities.

probably is due to the fact that the beam hits the optical elements inside the objective causing internal reflection. Thus, by carefully choosing the aperture size and implementing a hybrid approach in the simulation and experiment, we achieve high-fidelity TopHat patterns through the high NA objective.

4.4 Conclusion and outlook

In conclusion, we successfully produced the TopHat intensity pattern through a high NA objective as an important first step of single-shot ablation studies using spatially shaped beams. To our knowledge, this has been achieved for the first time. In the ablation community, creating high-fidelity custom shaped intensity with a tight focus at the Target plane has eluded experimental efforts. This is due to the fact that the GS algorithm is used to calculate the kinoforms [25], which creates undesirable speckle in the patterns. An accurate calibration of the SLM is also crucial as the calculated kinoforms are highly complex.

In our experiments, we typically use a pulsed laser system[6] with a bandwith of 10 nm. Due to the long focal lengths of the lenses[7] we use in the 4-f system, we are in the Fraunhofer diffraction regime [26], meaning different wavelengths within the bandwidth experience different magnifications. A narrow spread in the wavelength spectrum, therefore results in a superposition of the TopHat patterns with slightly different magnifications. The finite bandwidth of the laser thus creates smoother edges in the pattern. However, the TopHat patterns we use in the simulation already have smoother edges, shown in Fig. 4.3(c) and (d), so the effects on the edges are expected to be negligible. Therefore, our results are directly applicable to the ablation studies.

As an outlook, we see several possible improvements. First, the feedback loop [37] is necessary to experimentally realize the TiltedHat pattern as the intensity gradient along the pattern degrades the pattern due to the angle dependent diffraction efficiency of the SLM. The lenses in the 4-f system have to be changed so that the whole light field goes through the back aperture of the objective, which will significantly improve the efficiency of the TopHat/TiltedHat pattern. With these improvements, our system will be able to effectively and precisely shape laser beams for ablation.

[6] Hurricane, Spectra-Physics with λ_0=800 nm, $\Delta\lambda_{\mathrm{FWHM}}$=10 nm
[7] f_1=250 mm and f_2=450 mm

Bibliography

[1] M. Malinauskas, A. Zukauskas, S. Hasegawa, Y. Hayasaki, V. Mizeikis, R. Buividas, and S. Juodkazis, "Ultrafast laser processing of materials: from science to industry," Light Sci. Appl. **5**, e16133 (2016).

[2] M. Schmidt, M. Zah, L. Li, J. Duflou, L. Overmeyer, and F. Vollertsen, "Advances in macro-scale laser processing," CIRP Annals **67**, 719–742 (2018).

[3] L. Jiang, A.-D. Wang, B. Li, T.-H. Cui, and Y.-F. Lu, "Electrons dynamics control by shaping femtosecond laser pulses in micro/nanofabrication: modeling, method, measurement and application," Light Sci. Appl. **7**, 17134 (2018).

[4] C. A. Mack, "Fifty Years of Moore's Law," IEEE Transactions on Semiconductor Manufacturing **24**, 202–207 (2011).

[5] Z. Wang, T. Chen, and H. Zheng, "Wafer cutting method and a system thereof," (2011).

[6] J. v. Borkulo, P. Verburg, and R. v. d. Stam, "Multi Beam Full Cut Dicing of Thin Si IC Wafers," in "2017 IEEE 67th Electronic Components and Technology Conference (ECTC)," (2017), pp. 1817–1822.

[7] D. A. Willis and X. Xu, "Transport Phenomena and Droplet Formation During Pulsed Laser Interaction With Thin Films," Journal of Heat Transfer **122**, 763–770 (2000).

[8] M. Pasienski and B. DeMarco, "A high-accuracy algorithm for designing arbitrary holographic atom traps," Opt. Express **16**, 2176–2190 (2008).

[9] P. S. Salter and M. J. Booth, "Adaptive optics in laser processing," Light Sci. Appl. **8**, 110 (2019).

[10] F. M. Dickey, *Laser Beam Shaping* (CRC Press, 2014), 2nd ed.

[11] A. Mohl, S. Kaldun, C. Kunz, F. A. Muller, U. Fuchs, and S. Graf, "Tailored focal beam shaping and its application in laser material processing," J. Laser Appl. **31**, 042019 (2019).

[12] S. Matsuo, S. Juodkazis, and H. Misawa, "Femtosecond laser microfabrication of periodic structures using a microlens array," Appl. Phys. A **80**, 683–685 (2005).

[13] H. Zhang, "Single-shot femtosecond laser ablation on the nanoscale," Ph.D. thesis, Utrecht University (2013).

[14] A. A. Kuchmizhak, A. P. Porfirev, S. A. Syubaev, P. A. Danilov, A. A. Ionin, O. B. Vitrik, Y. N. Kulchin, S. N. Khonina, and S. I. Kudryashov, "Multi-beam pulsed-laser patterning of plasmonic films using broadband diffractive optical elements," Opt. Lett. **42**, 2838–2841 (2017).

[15] S. Syubaev, A. Porfirev, A. Zhizhchenko, O. Vitrik, S. Kudryashov, S. Fomchenkov, S. Khonina, and A. Kuchmizhak, "Zero-orbital-angular-momentum laser printing of chiral nanoneedles," Opt. Lett. **42**, 5022–5025 (2017).

[16] D. Pavlov, S. Gurbatov, S. I. Kudryashov, P. A. Danilov, A. P. Porfirev, S. N. Khonina, O. B. Vitrik, S. A. Kulinich, M. Lapine, and A. A. Kuchmizhak, "10-million-elements-per-second printing of infrared-resonant plasmonic arrays by multiplexed laser pulses," Opt. Lett. **44**, 283–286 (2019).

[17] S. Campbell, S. M. F. Triphan, R. El-Agmy, A. H. Greenaway, and D. T. Reid, "Direct optimization of femtosecond laser ablation using adaptive wavefront shaping," J. Opt. A: Pure Appl. Opt. **9**, 1100–1104 (2007).

[18] J. Liang, R. N. Kohn, Jr., M. F. Becker, and D. J. Heinzen, "High-precision laser beam shaping using a binary-amplitude spatial light modulator," Appl. Opt. **49**, 1323–1330 (2010).

[19] P. Zupancic, P. M. Preiss, R. Ma, A. Lukin, M. E. Tai, M. Rispoli, R. Islam, and M. Greiner, "Ultra-precise holographic beam shaping for microscopic quantum control," Opt. Express **24**, 13881–13893 (2016).

[20] G. Lazarev, P.-J. Chen, J. Strauss, N. Fontaine, and A. Forbes, "Beyond the display: phase-only liquid crystal on Silicon devices and their applications in photonics [Invited]," Opt. Express **27**, 16206–16249 (2019).

[21] R. J. Beck, J. P. Parry, W. N. MacPherson, A. Waddie, N. J. Weston, J. D. Shephard, and D. P. Hand, "Application of cooled spatial light modulator for high power nanosecond laser micromachining," Opt. Express **18**, 17059–17065 (2010).

[22] M. Silvennoinen, J. Kaakkunen, K. Paivasaari, and P. Vahimaa, "Parallel femtosecond laser ablation with individually controlled intensity," Opt. Express **22**, 2603–2608 (2014).

[23] J. Houzet, N. Faure, M. Larochette, A.-C. Brulez, S. Benayoun, and C. Mauclair, "Ultrafast laser spatial beam shaping based on Zernike polynomials for surface processing," Opt. Express **24**, 6542–6552 (2016).

[24] T. Hafner, J. Heberle, D. Holder, and M. Schmidt, "Speckle reduction techniques in holographic beam shaping for accurate and efficient picosecond laser structuring," J. Laser Appl. **29**, 022205 (2017).

[25] T. Hafner, J. Strauß, C. Roider, J. Heberle, and M. Schmidt, "Tailored laser beam shaping for efficient and accurate microstructuring," Appl. Phys. A **124**, 111 (2018).

[26] J. W. Goodman, *Introduction to Fourier Optics* (W. H. Freeman, 2017), 4th ed.

[27] A. L. Gaunt and Z. Hadzibabic, "Robust Digital Holography For Ultracold Atom Trapping," Sci. Rep. **2**, 721 (2012).

[28] C. Zhang, Y. Hu, W. Du, P. Wu, S. Rao, Z. Cai, Z. Lao, B. Xu, J. Ni, J. Li, G. Zhao, D. Wu, J. Chu, and K. Sugioka, "Optimized holographic femtosecond laser patterning method towards rapid integration of high-quality functional devices in microchannels," Sci. Rep. **6**, 33281 (2016).

[29] M. Mitchell, *An Introduction to Genetic Algorithms* (MIT, 2018).

[30] M. Clark and R. Smith, "A direct-search method for the computer design of holograms," Optics Communications **124**, 150–164 (1996).

[31] V. Boyer, C. M. Chandrashekar, C. M. Foot, and Z. J. Laczik, "Dynamic optical trap generation using FLC SLMs for the manipulation of cold atoms," Journal of Modern Optics **51**, 2235–2240 (2004).

[32] D. Bowman, T. L. Harte, V. Chardonnet, C. D. Groot, S. J. Denny, G. L. Goc, M. Anderson, P. Ireland, D. Cassettari, and G. D. Bruce, "High-fidelity phase and amplitude control of phase-only computer generated holograms using conjugate gradient minimisation," Opt. Express **25**, 11692–11700 (2017).

[33] D. Mikhaylov, B. Zhou, T. Kiedrowski, R. Mikut, and A.-F. Lasagni, "High accuracy beam splitting using spatial light modulator combined with machine learning algorithms," Optics and Lasers in Engineering **121**, 227–235 (2019).

[34] HOLOEYE Photonics AG, *PLUTO: Device Operating Instructions*, v1.3.2 ed. (2013).

[35] D. Engström, M. Persson, J. Bengtsson, and M. Goksör, "Calibration of spatial light modulators suffering from spatially varying phase response," Opt. Express **21**, 16086–16103 (2013).

[36] J. L. M. Fuentes, E. J. Fernández, P. M. Prieto, and P. Artal, "Interferometric method for phase calibration in liquid crystal spatial light modulators using a self-generated diffraction-grating," Opt. Express **24**, 14159–14171 (2016).

[37] G. D. Bruce, M. Y. H. Johnson, E. Cormack, D. A. W. Richards, J. Mayoh, and D. Cassettari, "Feedback-enhanced algorithm for aberration correction of holographic atom traps," J. Phys. B: At. Mol. Opt. Phys. **48**, 115303 (2015).

5 Summary and Outlook

Ultrafast laser ablation has opened up new possibilities to process materials with extreme precision and low collateral damage. Therefore its potential applications in industry can be wide-ranging. Currently, it is already being used for instance in ocular surgery and silicon wafer dicing as mentioned in Chapter 3 and Chapter 4 of this thesis. However, ablation is often utilized based on a trial and error approach, without fully understanding the main mechanism behind the material removal. In the work described in this thesis, we elucidate key aspects of the physics of material removal by using time-resolved transient reflectivity microscopy combined with spatial beam shaping. The materials we study in this thesis are water and gel as they are simple substitutes to study the ablation of tissue. As discussed in Chapter 1, the process behind femtosecond laser light-matter interaction is well separated in time scale, leading to a compartmentalization of the problem. In other words, since the underlying processes follow each other in a successive manner, understanding one is the starting point to understand the others. Within this context, the main ablation features we study with our setup are the expansion of the ablation plume and the surrounding shockwave-like feature.

In Chapter 2, we use two excitation spots simultaneously at a water/air interface and change the distance between them using a spatial light modulator (SLM). To realize this with traditional optical elements would be exceedingly complicated. This method enables us to record a strong stationary shock between the spots and map out the velocity field of the gas front, even when the individual shocks themselves are hard to detect. Based on the length of the strong shock, we measure the velocity field at two different pulse energies. Remarkably the velocity after 9ns of the expansion hardly depends on the absorbed energies. A scaling argument, combined with a FDTD calculation points to a clear deviation from the standard Sedov-Taylor model often used to describe the plume expansion.

An important quantity in ablation studies is the amount of removed material. If the amount of removed material is known, one can gain insight into

the dominant processes during material removal, such as evaporation, liquid motion and resolidification. However, in the case of liquid materials, this presents a challenge as the surface recovers after each excitation. To solve this problem, we study the ablation of gel in Chapter 3, as with a gel, a crater will remain visible in the aftermath. We measure the transient behavior of both gel and water over a wide range of pulse energies at a set delay time. We find an extremely similar expansion dynamics, which enables us to estimate the removed material during water ablation based on the gel ablation aftermath. From those measurements and FDTD calculations, we estimate the amount of removed material and calculate the energy absorbed by the material. We find that the removed mass and the absorbed energy follow a similar trend. From this, we argue that the (highly supersonic) expansion velocity of the ablation plume is almost independent of the laser pulse energy. However, we currently do not have the experimental techniques to directly observe the (vertical) expansion of the plume.

As liquid motion inside the molten layer of the material contributes to the material removal process, it would be advantageous to control this flow. One could control and study the flow using spatially shaped laser beams, such as the TiltedHat beams discussed in Chapter 4. Therefore, we develop a beam shaping method for laser ablation with high NA optics. We demonstrate high-fidelity TopHat patterns as a first step towards reaching this goal.

In future research, we suggest to use spatial beam shaping to enable side imaging under strong focusing conditions. This can be achieved by creating a strongly elongated pump focus, with a flat intensity profile in the long direction. This will enable a direct measurement of the vertical expansion velocity of the ablation plume. Thus, the beam shaping techniques developed in this thesis give new prospects for future studies, and new insights into the dynamics during ultrafast femtosecond laser ablation are certainly on the horizon.

Samenvatting in het Nederlands

Ultrasnelle laser ablatie maakt het mogelijk om materialen om te bewerken met extreme nauwkeurigheid en met weinig bijkomende schade. Er kan daarom een breed toepassingsgebied in de industrie worden verwacht. Op dit moment wordt ultrasnelle laser ablatie al gemaakt in oogchirurgie en voor het op maat snijden van computerchips, zoals besproken in Hoofdstukken 3 en 4 van dit proefschrift. Hoewel ablatie dus al wordt toegepast, gebeurd dit vaak zonder dat er een goed begrip is van welk mechanisme nu precies verantwoordelijk is voor het verwijderen van het materiaal. In dit proefschrift maken we de belangrijkste aspecten van de natuurkunde van laser ablatie zichtbaar, met behulp van onze ablatie microscoop (een tijdsopgeloste reflectiviteitsmicroscoop) in combinatie met ruimtelijke bundel vorming. We hebben ervoor gekozen om onze experimenten te doen met water en gel, omdat deze kunnen worden gezien als ver'e'envoudigde versie van biologisch weefsel.

Zoals we in Hoofdstuk 1, kan femtoseconde laser ablatie worden beschreven dus processen die gescheiden zijn in de tijd. Met andere woorden, de belangrijke processes vinden na elkaar plaats en niet tegelijkertijd. Dat betekent dat als we 'e'en proces begrijpen, we de beginvoorwaarden voor het volgende proces kennen. In dit werk concentreren we ons bij ons experimentele werk op de expansie van de ablatie pluim en op de schokgolfachtige ringen die we daar omheen waarnemen.

In Hoofdstuk 2 gebruiken we twee laser foci om tegelijk ablatie te induceren op twee plekken om een water oppervlak. Met behulp van een ruimtelijk licht modulator kunn we de afstand tussen deze twee foci eenvoudig veranderen, iets wat met traditionele optische element zeer ingewikkeld zou zijn. De twee ablatiepluimen verdringen de omringende lucht en waar deze twee luchtstromingen op elkaar botsen, onstaat een sterke, stationaire schokgolf, zelfs wanneer de stromingssnelheid ten gevolge van de individuele ablatiepluimen subsonisch is. Door de lengte van deze stationaire schokgolf te meten als functie van de afstand tussen de twee foci, kunnen we het radiele snelheidsprofiel in de lucht rond de ablatiepluim in kaart brengen. Dit snelheidsprofiel blijkt slecht zwak

af te hangen van de pulsenergie, dwz, de snelheidsprofielen zijn voor twee verschillende pulsenergieen, op een schaling van de ruimtelijke as, nagenoeg gelijk. Deze schalingswet lijkt inconsistent met het eenvoudige Sedov-Taylor model dat vaak voor de expansie van de ablatiepluim wordt gebruikt.

Een belangrijke grootheid bij het bestuderen van ablatie is natuurlijk de hoeveelheid materiaal die is verwijderd. Kennis over deze hoeveelheid geeft inzicht in de dominant processen die verantwoordelijk zijn voor het verwijderen van het materiaal, zoals verdamping, vloeistofstroming en stolling. Bij het bestuderen van ablatie van een vloeistof, zoals water, is het echter moeilijk om dit te meten. Het oppervlak herstelt zich immers snel na de ablatie weer. Om deze reden bestuderen we in Hoofstuk 3 de ablatie van gel, aangezien in dat geval een krater zichtbaar zal blijven na ablatie. Om zeker te zijn dat het water en de gel zich vergelijkbaar gedragen, meten we over een groot gebied van pulsenergieen gedrag van de oppervlakte reflectiviteit in onze ablatie microscoop. Het blijkt dat de expansie van de ablatiepluim bij water en gel inderdaad zeer veel op elkaar lijken. Hieruit concluderen we dat we, als we bij gel metingen doen aan de krater, we mogen veronderstellen dat water zich vergelijkbaar gedraagt. Met andere woorden, we meten de hoeveel gel die is verwijderd en concluderen dat dat ook de hoeveelheid water is die is verwijderd. Vervolgens berekenen we voor het geval van water hoeveel laser energie er als functie van de laser pulsenergie wordt geabsorbeerd, met behulp van een geavanceerd FDTD model wat in onze groep voor water is opgesteld. We vergelijken deze energie die door het water is geabsorbeerd met de massa die is verwijderd en vinden dat deze twee grootheden over een groot energiegebied precies op elkaar liggen, dwz de verwijderde massa lijkt recht evenredig met de geabsorbeerde energie. Dit suggereert dat de expansie snelheid van de ablatie pluim (vrijwel) onafhankelijk is van de geabsorbeerde energie. Het zou daarom zeer interessant zijn om deze snelheid met een onafhankelijk methode te meten, we hebben echter op dit moment geen experimentele techniek om de verticale snelheidscomponent te bepalen.

Aangezien vloeistofstroming in de toplaag van het geableerde materiaal significant bijdragen aan verwijderen van massa, zou het goed zijn als we deze stroming zouden kunnen sturen of in ieder geval zou kunnen bestuderen. Daarvoor kunnen we ruimtelijk gevormde bundel profielen gebruiken. Om dit mogelijk te maken hebben we een methode ontwikkeld om met behulp van een ruimtelijke licht modulator de gewenste bundelprofielen te realiseren. Bijzonder hierbij is dat we deze profielen, anders dan in voorgaand werk, kunnen

projecteren door een microscoop objectief met een zeer hoge numerieke apertuur. We laten zien dat we zogenaamde Hoge Hoed profielen en Scheve Hoed profielen kunnen maken. Dit is een belangrijk stap richting het gebruik van deze profielen in ablatie experimenten.

Voor nieuwe onderzoek stellen we voor om ruimtelijke bundel vorming te gebruiking om de ablatie bundel om te vormen tot een lijn profiel, waarbij de intensiteit constant langs de lijn. Het grote voordeel van deze techniek is dat als we langs de lijn kijken, de ablatiepluim diep genoeg zal zijn om een schaduw te werpen. We zullen op die wijze dus de expansie van de pluim in zijaanzicht kunnen meten. Tegelijkertijd kunnen we echter loodrecht op de lijn nog steeds een strak focus realiseren, iets wat in normale zijaanzicht experimenten onmogelijk is. De bundelvormingstechnieken die we in dit proefschrift hebben ontwikkeld, kunnen we dus gebruiken om fundamentele nieuwe inzichten te verkrijgen over laser ablatie, onder condities die direct relevant zijn voor toepassingen.

Acknowledgements

During my PhD, I encountered a situation that I had to restart my whole PhD and finish it within one and half year. Many people thought accomplishing it would be impossible and even attempting it would be a fool's errand. I don't blame them for thinking like that as even completing PhD within 4-years is a considerable task. Then how come one can accomplish such a crazy task given a crazy short, should I say ultra-fast, amount of time? Certainly not all by himself. Fortunately, I had a great team, best team anyone could ask for, who supported me in every possible way during this extraordinary time of my life. I would like to acknowledge their trust during uncertain times, help when I needed most, advise that helped me get through crucial moments and most of all, their unwavering support.

First of all, I would like to thank Allard, my promotor and mentor. I remember when I first time "met" you during Skype call for a PhD position interview. I was attending IEEE magnetics summer school in the US at that time. I was quite nervous during the call because I didn't expect it happen so soon. You looked calm yet had this scary looking eyebrows that frightened me a little bit. After four years, I can now safely say my first impressions were quite wrong. You are a caring person with a good heart, who always looks after his students. You are never authoritarian and always gives your students freedom to make their own choices, which I think the most important trait in a supervisor. I could not emphasize enough the enormous influence you had on my personal development, which could be worth several PhDs. I could not thank you enough!

Dries, my teacher and my friend, I do not know where to begin. You are the one who took me in your group when times were most uncertain. I hope that I have not made you regret that decision even once. Looking back time we worked together, things we accomplished in this short amount of time are mind-blowing: PhD thesis starting from zero, 2 publications, and one successful grant application that provided a life line in our research project with a brand new laser and a PhD student. Your contribution to all these is

gigantic. I vividly remember the morning you told me the grant application was awarded. It meant a lot to me, probably even more than getting a PhD. It made a possible that our research line will live on specially it was during the time when our beloved laser Hurricane was in its death bed. All of our effort, endless work, and constant challenges we faced worth it because of it. Not all of our work was about facing hardships, there were many happy moments we had together. It was pure joy discussing with you many weird things ranging from kung-fu, MMA, Rick and Morty, my bad taste in music to physics. Your knowledge in physics fundamentals is amazing. It is quite a rare thing to have a such good grasp of fundamentals even for theoreticians. No wonder your PhD thesis is full of theory work.

Javi, my dearest friend and our "laser whisperer", I do not know what to say except thank you, thank you, thank you! This thesis is only possible because of your tremendous help. Your work during your stay in Utrecht provided the backbone of the thesis. I enjoyed so much performing experiments with you. You taught me lots of things even from basics such as laser alignment to FDTD modeling and ablation physics. You were always there whenever I had a question, and you clearly, patiently explained me things, which I appreciate a lot. Besides physics, I value most your advice whenever I had an issue outside of the lab, especially at last stages of writing the thesis. It really helped me to focus on what is important. Also your work ethic and your focus on efficiency are simply amazing. Working with you definitely helped me to get out of my Japanese work mentality.

Cees, Dante, and Paul, the dynamic trio of Nanophotonics! Your contribution to the project is indisputable. Cees, our laser technician, I can not thank you enough for helping me to maintain the Hurricane as it got broken down multiple times. You came even during your holidays to help me on Hurricane. You promptly made a call to Belgium to invite the technician from Spectra Physics. You understood the situation when it mattered most. I can not forget that. I remember when our laser finally passed away and we all were laughing there because it happened just after Dries got the grant. I guess we are the ones who got the last laugh after all. I wish you long and happy retirement! Dante, our electronics technician and one of the nicest person I ever met, I thank you for your patience and help during all these years. I asked you to make me things I often did not use in the end. Please forgive me. I enjoyed a lot our casual discussions on many things like USA, Trump, making delicious spaghetti etc. Paul, our mechanics technician and my go

to bike guy, I appreciate a lot for your prompt help whenever I needed you to make things for the experiments. Also I could not forget many times you helped me to fix my bike. People joked about it but you have no idea how much it was important for me. Having one less thing to worry about when I had thousand issues to deal with really helped me a lot to focus on my thesis. It was tremendous help. I could not thank you enough!

Akash, how can I forget you! Your place here is well deserved. I remember well when you first came from the Netherlands to Japan with Gerrit. We had a lot of fun every time you visited. During many karaoke outings, you told me all those wonderful things about the Netherlands and eventually convinced me to pursue PhD in the Netherlands. I am so glad that I followed your advice. You also gave me valuable advice that helped me a lot on my personal development. Thank you!

Doing PhD is not just all about work. I created many nice memories with my colleagues from Nanophotonics group. I had two great roommies in my office, Bohdan and Jasper, who are so much fun to hang out with, discussing countless topics math, physics, politics and other things I can't mention here. Jasper, one of the smartest guys in our group, I enjoyed a lot hanging out with you even though you joined our room during my final years. I will never forget your initiation to our room. It was so much fun. Bohdan, true "mujik" in our group, I really like your honesty and straight shooter mentality. We often tend to sit in the office silently, completely absorbed in our work yet when we talk, we talk hours non-stop. I really enjoyed it. Sebas, Arjon, and Pritam, our athletic neighbors, I had a lot of fun hanging out with you from exercising outside, swimming in a lake, playing football, bowling, bouldering, and so much more. Karindra, a musician of our group and one of the kindest people I ever met, you are the one who would listen to me and gave me a consultation when I was down. It was tremendous help and I really appreciate it. Jeroen and Marcel, two very cool nerds of our group and great partners in discussing unorthodox subjects, you always helped me when I had a question and need. Jeroen, I remember our "museum dates" when I was still in Zeist, it was quite fun. Mijke, our beloved secretary, I really like your great sense of humor, which often made my day. You always prepared to help us, poor helpless PhDs. We are really lucky to have you in our group! Of course, there are countless other people from Nanophotonics who made my time here unforgettable experience: Abi, Anna, Aquiles, Charly, Dorian, Gijs, Jacob, Jin, Kevin, Kuang, Ole, Peter, Pegah, Sandy, Sanli, Sergei, Sid, Tang, Zhu, XiaoXing. Thank you all!

Finally, I would like to thank my parents for their endless love and support!

Curriculum Vitae

Dashdeleg Baasanjav was born on 19 August, 1987 in Ulaanbaatar, Mongolia. He graduated from Ulaanbaatar No. 1 secondary school in 2005, after which he attended National University of Mongolia for two years with a national government scholarship. In 2008, he won Japanese Government Scholarship (Monbukagakusho) to study at Tohoku University, Japan. He completed his Bachelor's and Master's degree in 2013 and 2015 respectively at Institute of Materials Research, Tohoku University, under the supervision of Prof. Gerrit Bauer and Dr. Oleg Tretiakov. During his Master's research, he worked on condensed matter theory, specifically he completed numerical calculations of magneto-electric effect in a three dimensional topological insulator slab and analytic calculations of the Barnett effect in a rotating two dimensional free electron gas. From 2016, he started his PhD at Nanophotonics group of Debye Institute for Nanomaterials Science, Utrecht University.